

## Assessing the Equatorial Long-Wave Approximation: Asymptotics and Observational Data Analysis\*

H. REED OGROSKY

*Department of Mathematics, University of Wisconsin–Madison, Madison, Wisconsin*

SAMUEL N. STECHMANN

*Department of Mathematics, and Department of Atmospheric and Oceanic Sciences, University of Wisconsin–Madison, Madison, Wisconsin*

(Manuscript received 4 March 2015, in final form 19 August 2015)

### ABSTRACT

Equatorial long-wave theory applies where a small horizontal aspect ratio between meridional and zonal length scales is assumed. In an idealized setting, the theory suggests that (i) meridional wind is small, (ii) geostrophic balance holds in the meridional direction, and (iii) inertio-gravity waves are small in amplitude or “filtered out.” In this paper a spectral data analysis method is used to quantitatively assess the spatial and temporal scales on which each of these aspects of long-wave dynamics is observed in reanalysis data. Three different perspectives are used in this assessment: primitive variables, characteristic variables, and wave variables. To define each wave variable, the eigenvectors and theoretical wave structures of the equatorial shallow-water equations are used. Evidence is presented that the range of spatial and temporal scales on which long-wave dynamics holds depends on which aspect of the dynamics is considered. For example, while meridional winds are an order of magnitude smaller than zonal winds over only a very narrow range of spatial scales (planetary wavenumber  $|k| \lesssim 1$ ), an examination of meridional geostrophic balance and inertio-gravity waves indicates long-wave dynamics for a broader range of scales ( $|k| \lesssim 4$ ). A simple prediction is also presented for this range of scales based on physical and mathematical reasoning.

### 1. Introduction

One type of “balanced dynamics” in the tropical atmosphere occurs on planetary zonal scales; accordingly it is called the equatorial long-wave dynamics (Heckley and Gill 1984; Majda 2003; Majda and Klein 2003).<sup>1</sup>

<sup>1</sup> Another class of balanced dynamics in the tropics includes a variety of weak temperature gradient (WTG) approximations (Charney 1963; Sobel et al. 2001; Majda and Klein 2003; Stechmann and Stevens 2010).

\* Supplemental information related to this paper is available at the Journals Online website: <http://dx.doi.org/10.1175/JAS-D-15-0065.s1>.

*Corresponding author address:* H. Reed Ogrosky, Department of Mathematics, University of Wisconsin–Madison, 480 Lincoln Dr., Madison, WI 53706-1325.  
E-mail: ogrosky@math.wisc.edu

These dynamics are marked by several related characteristics, including small meridional winds, geostrophic balance in the meridional direction, and inertio-gravity waves of small amplitude. Theories that exploit an assumed small ratio of meridional to zonal length scales suggest that these dynamics are valid on “long” zonal and temporal scales.

The main goal of this paper is to assess how long the zonal and temporal scales must be in order for equatorial long-wave dynamics to exist. Such an assessment is important as many low-dimensional models of planetary-scale phenomena in the tropical atmosphere are derived in part using the long-wave approximation. Examples include models of equatorial waves and their interactions (Majda and Biello 2003) and the Madden–Julian oscillation (MJO; Majda and Biello 2004; Biello and Majda 2005; Majda and Stechmann 2009). Other models incorporate a steady-state version of the long-wave theory, such as models for the Walker circulation (Gill 1980; Stechmann and Ogrosky 2014) and El Niño–Southern Oscillation (ENSO; Cane and Zebiak 1985).

In addition to justifications based on scale analysis or formal asymptotics, there are rigorous mathematical proofs of the convergence to long-wave dynamics under the appropriate limit (Dutrifoy and Majda 2006; Dutrifoy et al. 2009). What is more, fast-wave averaging has been used to show the existence of balanced dynamics even with imbalanced initial conditions in the tropics (Dutrifoy and Majda 2007). These results have been proven for the equatorial shallow-water equations; a remaining mathematical challenge is to prove similar results for the three-dimensional primitive equations.

Using observational data, assessing the scales on which long-wave dynamics exist is fraught with challenges. A substantial disconnect exists between tropical dynamics in nature and in idealized fluid dynamics models. For example, in idealized fluid dynamics models, the effects of water vapor and convection must be included in some way, perhaps through an imposed forcing or a parameterization. In nature, in contrast, water vapor and convection are part of a highly complex turbulent dynamics. Also, idealized models typically either neglect forcing or prescribe forcing functions of a particular order of magnitude; the magnitude of forcing in nature need not satisfy such constraints. For these reasons and others, one might not expect to be able to accurately assess the validity of the long-wave approximation using observational or reanalysis data. Nevertheless, it will be shown below that a sensible assessment can in fact be made.

This assessment is achieved by applying a spectral data analysis and wave projection technique introduced recently in Stechmann and Majda (2015). Spatial projections onto theoretical basis functions in  $x$ ,  $y$ ,  $z$ , and  $t$  are used. Previous studies have also used some combination of spatial projections (e.g., Wheeler and Kiladis 1999) and many others have utilized Fourier modes in  $x$  and  $t$ . Yang et al. (2003, 2007) and Gehne and Kleeman (2012) utilized parabolic cylinder functions in  $y$ , and projecting onto vertical basis functions has a long history (e.g., Kasahara 1976; Kasahara and Puri 1981; Fulton and Schubert 1985). The spectral approach employed here uses a unique projection in the vertical direction that isolates the first baroclinic mode and does not include the stratosphere. Combined with projections in the other directions, this approach systematically isolates (i) the first baroclinic mode, (ii) individual meridional modes, and (iii) individual zonal and temporal Fourier modes in the data. This spectral isolation of spatiotemporal scales in each dimension allows for a clear assessment of the scales on which the dynamics are long-wave in character.

Wave amplitudes are also identified here for individual wave types, providing a systematic way to combine

data from multiple fields (such as wind and geopotential height) into a single meaningful multivariate field. This method was presented by Stechmann and Majda (2015) for the long-wave equations; here it is introduced for the traditional (i.e., no long-wave assumption) shallow-water equations as well.

Three perspectives will be used here, each corresponding to a different choice of model variables: (i) primitive ( $u$ ,  $v$ ,  $\theta$ ), (ii) characteristic ( $r$ ,  $l$ ,  $v$ ), and (iii) wave ( $K$ ,  $R_m$ , etc.). Each perspective is best suited to assessing a particular aspect of long-wave dynamics: primitive variables allow a direct assessment of small meridional winds  $v$  compared to zonal winds  $u$ , characteristic variables allow spectral assessment of meridional geostrophic balance, and wave variables allow direct assessment of the strength of each type of equatorial wave structure.

The rest of the paper is thus organized as follows. Section 2 contains a review of the equatorial long-wave approximation. A simple prediction is given of the scales on which this approximation may be expected to be valid based on physical and mathematical arguments. Section 3 describes the data and methods used for the observational data analysis. The data are then analyzed from three perspectives: (i) primitive variables, (ii) characteristic variables, and (iii) wave variables, in sections 4, 5, and 6, respectively. Some discussion of the results is given in section 7, and a summary of the main findings of the paper is given in section 8. Additional results from the viewpoint of wave variables can be found in the supplementary materials.

## 2. Background on the equatorial long-wave approximation

We begin with the linearized three-dimensional equations for a rotating hydrostatic Boussinesq fluid:

$$\partial_t U - \beta y V = -\partial_x P + S_U, \quad (2.1a)$$

$$\partial_t V + \beta y U = -\partial_y P + S_V, \quad (2.1b)$$

$$g \frac{\Theta}{\theta_{\text{ref}}} = \frac{\partial P}{\partial z}, \quad (2.1c)$$

$$\partial_t \Theta + W \frac{d\theta_{\text{bg}}}{dz} = S_\Theta, \quad (2.1d)$$

$$\partial_x U + \partial_y V + \partial_z W = 0, \quad (2.1e)$$

with rigid-lid boundary conditions at the top,  $z = H$ , and bottom,  $z = 0$ , of the troposphere. The variables  $\mathbf{U} = (U, V)$  and  $W$  are the  $(x, y)$  and  $z$  components of the winds, respectively;  $P$  is pressure; and  $\Theta$  is potential temperature. In addition,  $g$  is acceleration due to gravity,

$\beta$  is the variation of the Coriolis parameter with latitude,  $\theta_{\text{ref}}$  is a reference background potential temperature, and  $d\theta_{\text{bg}}/dz$  is the background vertical gradient of potential temperature. The source terms  $S_U$ ,  $S_V$ , and  $S_\theta$  represent forcing due to, for example, heating and cooling or dissipation; these terms could also contain contributions that represent the effects of nonlinear advection neglected in the linearized equations. The Boussinesq equations have been used as a starting point here for simplicity; a realistic anelastic atmosphere would lead to the same type of shallow-water system as the one derived below, but with modified vertical basis functions (e.g., Kasahara 1976; Kasahara and Puri 1981; Fulton and Schubert 1985).

*a. First baroclinic mode dynamics*

The rigid-lid boundary condition allows each of the fluid variables to be expanded in terms of its vertical basis components:

$$\mathbf{U}(x, y, z, t) = \sum_{j=0}^{\infty} \mathbf{u}_j(x, y, t) C_j(z),$$

$$\Theta(x, y, z, t) = \sum_{j=1}^{\infty} \theta_j(x, y, t) S_j(z), \tag{2.2a}$$

$$P(x, y, z, t) = \sum_{j=0}^{\infty} p_j(x, y, t) C_j(z),$$

$$W(x, y, z, t) = \sum_{j=1}^{\infty} w_j(x, y, t) S_j(z), \tag{2.2b}$$

where the vertical basis functions are

$$C_0(z) = 1, \tag{2.3a}$$

$$C_j(z) = \sqrt{2} \cos(\pi j z / H), \quad S_j(z) = \sqrt{2} \sin(\pi j z / H),$$

$$j = 1, 2, 3, \dots, \tag{2.3b}$$

and where analogous expansions apply for each of the source terms  $S_U$ ,  $S_V$ , and  $S_\theta$ . When (2.2) is substituted into (2.1), these equations can be projected onto each vertical mode resulting in a set of systems of equations, with one system describing the barotropic mode, another describing the first baroclinic mode, etc.

We restrict our attention to the linearized first-baroclinic-mode equations (dropping numerical subscripts):

$$\partial_t u - \beta y v - \partial_x \theta = S_u, \tag{2.4a}$$

$$\partial_t v + \beta y u - \partial_y \theta = S_v, \tag{2.4b}$$

$$\partial_t \theta - \frac{H}{\pi} \frac{d\theta_{\text{bg}}}{dz} (\partial_x u + \partial_y v) = S_\theta. \tag{2.4c}$$

Equations (2.4) can be nondimensionalized by

$$x = \frac{L_E}{\delta} x^*, \quad y = L_E y^*, \quad t = \frac{T_E}{\delta} t^*, \tag{2.5a}$$

$$u = \frac{L_E}{T_E} u^*, \quad v = \frac{L_E}{T_E} v^*, \quad \theta = \frac{HN^2 \theta_{\text{ref}}}{\pi g} \theta^*, \tag{2.5b}$$

$$S_u = \frac{\delta L_E}{T_E^2} S_u^*, \quad S_v = \frac{\delta L_E}{T_E^2} S_v^*, \quad S_\theta = \frac{\delta HN^2 \theta_{\text{ref}}}{\pi g T_E} S_\theta^*, \tag{2.5c}$$

where asterisks denote dimensionless quantities, and where

$$L_E = \sqrt{\frac{NH}{\pi \beta}}, \quad T_E = \sqrt{\frac{\pi}{NH \beta}}, \quad N^2 = \frac{g}{\theta_{\text{ref}}} \frac{d\theta_{\text{bg}}}{dz}, \tag{2.6}$$

are the meridional length scale, time scale, and buoyancy frequency squared, respectively. The scales in (2.6) are the natural, standard equatorial synoptic scales in the troposphere and  $\delta$  is an aspect ratio parameter discussed below. All parameter values are shown in Table 1. Note that we will take  $L_E = 1500$  km, corresponding to a characteristic velocity of roughly  $50 \text{ m s}^{-1}$  and an equivalent depth of roughly 260 m.

The aspect ratio  $\delta$  is typically treated in one of two ways. Setting  $\delta = 1$  and substituting (2.5) into (2.4) results in the dimensionless equations (dropping asterisks hereafter),

$$\partial_t u - yv - \partial_x \theta = S_u, \tag{2.7a}$$

$$\partial_t v + yu - \partial_y \theta = S_v, \tag{2.7b}$$

$$\partial_t \theta - \partial_x u - \partial_y v = S_\theta. \tag{2.7c}$$

System (2.7) will be referred to here as the “standard” system.

*b. Long-wave scaling in primitive variables*

For a general value of  $\delta$ , the dimensionless equations take the following form:

$$\delta \partial_t u - yv - \delta \partial_x \theta = \delta S_u, \tag{2.8a}$$

$$\delta \partial_t v + yu - \partial_y \theta = \delta S_v, \tag{2.8b}$$

$$\delta \partial_t \theta - \delta \partial_x u - \partial_y v = \delta S_\theta. \tag{2.8c}$$

If it is assumed that  $\delta \ll 1$ , each variable can then be expanded in powers of  $\delta$ :

$$u = u_0 + \delta u_1 + O(\delta^2), \quad v = v_0 + \delta v_1 + O(\delta^2),$$

$$\theta = \theta_0 + \delta \theta_1 + O(\delta^2). \tag{2.9}$$

Substitution of (2.9) into (2.8) results in, to leading order in  $\delta$ ,

TABLE 1. Values of scaling parameters and constants.

Parameter	Derivation	Value	Description
$\beta$		$2.3 \times 10^{-11} \text{ m}^{-1} \text{ s}^{-1}$	Variation of Coriolis parameter with latitude
$P_E$		40 000 km	Circumference of Earth
$\theta_{\text{ref}}$		300 K	Reference potential temperature
$g$		$9.8 \text{ m s}^{-2}$	Gravitational acceleration
$H$		16 km	Tropopause height
$d\theta_{\text{bg}}/dz$		$3.1 \times 10^{-3} \text{ K m}^{-1}$	Background potential temperature gradient
$N^2$	$(g/\theta_{\text{ref}})d\theta_{\text{bg}}/dz$	$10^{-4} \text{ s}^{-2}$	Buoyancy frequency squared
$L_E$	$\sqrt{NH/\pi\beta}$	1500 km	Equatorial length scale
$T_E$	$\sqrt{\pi/\beta NH}$	8 h	Equatorial time scale
	$L_E/T_E = NH/\pi$	$50 \text{ m s}^{-1}$	Horizontal velocity scale
	$HN^2\theta_{\text{ref}}/(\pi g)$	15 K	Potential temperature scale
	$c^2/g$	255 m	Geopotential height scale

$$v_0 = 0, \quad (2.10a)$$

$$yu_0 - \partial_y \theta_0 = 0, \quad (2.10b)$$

$$\partial_y v_0 = 0. \quad (2.10c)$$

Thus, one immediate consequence of this small- $\delta$  assumption is that  $v = O(\delta)$ , while  $u$  and  $\theta$  are  $O(1)$  quantities that satisfy meridional geostrophic balance in (2.10b) to leading order. For this reason  $v$  is typically rescaled by

$$v = \delta v', \quad (2.11)$$

resulting in

$$\partial_t u - yv' - \partial_x \theta = S_u, \quad (2.12a)$$

$$\delta^2 \partial_t v' + yu - \partial_y \theta = \delta S_v, \quad (2.12b)$$

$$\partial_t \theta - \partial_x u - \partial_y v' = S_\theta. \quad (2.12c)$$

Retaining only leading-order terms in  $\delta$  results in the commonly used form of the long-wave equations:

$$\partial_t u - yv' - \partial_x \theta = S_u, \quad (2.13a)$$

$$yu - \partial_y \theta = 0, \quad (2.13b)$$

$$\partial_t \theta - \partial_x u - \partial_y v' = S_\theta. \quad (2.13c)$$

This assumption of small  $\delta$  is referred to as the ‘‘equatorial long wave,’’ or simply ‘‘long wave,’’ approximation.

### c. Estimating long-wave scales from theory

A natural question to ask is ‘‘Over what range of spatial and temporal scales can the long-wave equations [(2.13)] be expected to accurately describe the linear dynamics of the first baroclinic mode of the tropical atmosphere?’’ Before turning to reanalysis data to address this question, this range of spatiotemporal scales is briefly estimated in two ways from theoretical considerations.

One crude estimate may be found through the following straightforward physical considerations. It is reasonable to assume that the small aspect ratio  $\delta$  depends on the dimensionless zonal wavenumber  $k$ :

$$\delta = \frac{y_{\text{ref}}}{x_{\text{ref}}} = \frac{L_E}{P_E/|k|}, \quad (2.14)$$

where  $P_E$  is the circumference of Earth. The long-wave approximation  $\delta \ll 1$  is then expected to be valid for zonal wavenumbers satisfying

$$|k| \ll P_E/L_E. \quad (2.15)$$

To estimate a specific range of wavenumbers and frequencies for which condition (2.15) is satisfied, it is helpful to define a ‘‘largest acceptable ratio’’  $\delta_{\text{max}}$  of the left-hand to right-hand sides of (2.15). In other words, we say that condition (2.15) is met for all  $k$  that satisfy

$$|k| \leq \delta_{\text{max}} P_E/L_E, \quad (2.16)$$

respectively. We note that there is no one ‘‘correct’’ choice for  $\delta_{\text{max}}$ , but in atmospheric contexts, taking  $\delta_{\text{max}} = O(10^{-1})$  is fairly common [see, e.g., Majda and Klein (2003) or chapter 5 of Vallis (2006)]. For the rest of this paper, results corresponding to  $\delta_{\text{max}} = 0.3$  are highlighted, though we emphasize that every contour in each power spectrum ratio plot corresponds to a value of  $\delta_{\text{max}}$ . With  $P_E \approx 40\,000$  km and taking  $\delta_{\text{max}} = 0.3$ , condition (2.16) is satisfied for  $-8 \leq k \leq 8$ .

Similarly, we may expect that long-wave dynamics will only hold for frequencies  $\omega$  (where  $\omega$  is the dimensionless frequency) such that  $\omega \leq \delta_{\text{max}}$ . With  $\delta_{\text{max}} = 0.3$  and  $T_E \approx 1/3$  days, we find  $\omega/T_E \leq 0.9$  cpd. Together then, we may expect that long-wave dynamics will hold on spatiotemporal scales where the wavenumbers and frequencies satisfy

$$-8 \leq k \leq 8, \quad \omega/T_E \leq 0.9 \text{ cpd}, \quad (2.17)$$

respectively. Note that of course the endpoints of the range in (2.17) are merely indicative of the spatial and temporal scales at which a transition from long-wave to non-long-wave dynamics can be expected and should not be taken to indicate an abrupt shift in dynamics.

A second, related estimate may be found through the following mathematical consideration. Solutions to (2.8) can be expressed as the superposition of individual Fourier components in space and time:

$$\begin{aligned} \hat{u}(k, y, \omega) \exp[i(\delta_k x - \delta_\omega t)], \quad \hat{v}(k, y, \omega) \exp[i(\delta_k x - \delta_\omega t)], \\ \hat{\theta}(k, y, \omega) \exp[i(\delta_k x - \delta_\omega t)], \end{aligned} \tag{2.18}$$

with

$$\delta_k = 2\pi k L_E / P_E, \quad \delta_\omega = 2\pi\omega. \tag{2.19}$$

In order for the long-wave approximation to hold, we require that variations in  $x$  and  $t$  be small [i.e., the coefficients of  $x$  and  $t$  in (2.18) must be small in magnitude]:

$$\delta_k \ll 1, \quad \delta_\omega \ll 1. \tag{2.20}$$

As before, an estimate of the range of wavenumbers and frequencies on which conditions (2.20) are met can be made by requiring  $\delta_k \leq \delta_{\max}$  and  $\delta_\omega \leq \delta_{\max}$ . With the values of  $L_E$ ,  $P_E$ , and  $\delta_{\max}$  used above, we find that

$$-1.3 \leq k \leq 1.3, \quad \omega / T_E \leq 0.14 \text{ cpd}, \tag{2.21}$$

where, of course, the wavenumber  $k$  may only take on integral values.

Figure 1 shows the regions of wavenumber–frequency space where conditions (2.17) and (2.21) are satisfied. The dispersion curves of some of the linear solutions to (2.7) are also shown. The first estimate [i.e., (2.17)] encompasses a broad range of wavenumbers and frequencies, including pieces of both the mixed Rossby-gravity (MRG) and inertio-gravity (IG) wave dispersion relations. The second estimate [i.e., (2.21)] is a much more restrictive assumption; the difference in dimension size of the two regions is a factor of  $2\pi$  in both wavenumber and frequency. Such a distinction is typically not important for purposes where a qualitative, order-of-magnitude assessment of long-wave scales is sufficient but is large enough in extent to be of interest in a quantitative assessment. The smaller estimate associated with conditions (2.21) will be overlaid onto some of the data analysis results displayed using wavenumber–frequency plots in the following sections.

We pause to briefly discuss the underlying difference between these two perspectives. In the first perspective,

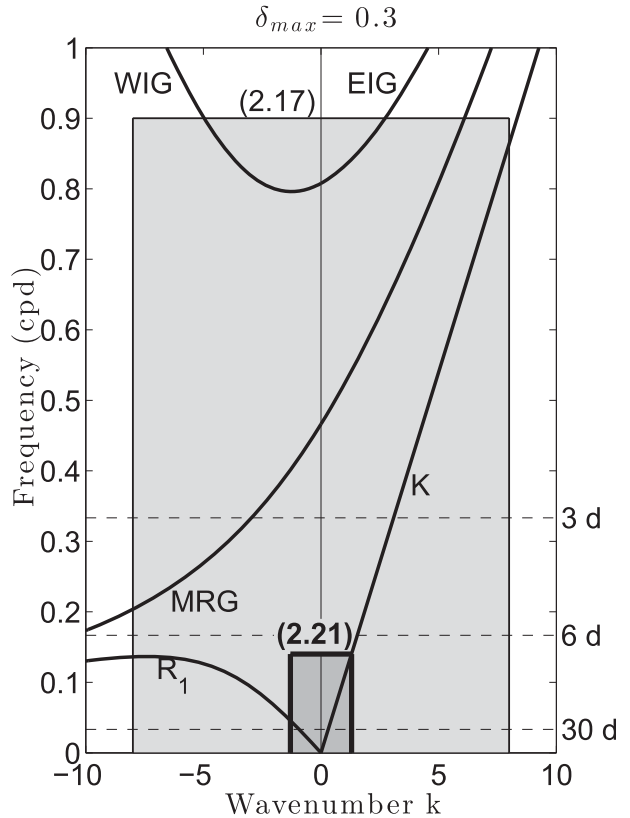


FIG. 1. Regions in wavenumber–frequency space where conditions (2.17) (light shading) and (2.21) (dark shading) are satisfied. Dispersion relations for linear solutions to (2.7) are depicted by solid lines.

the zonal-to-meridional aspect ratio has been defined by comparing a whole zonal wavelength with the meridional trapping scale  $L_E$ ; in the second perspective, only a fraction (specifically,  $1/2\pi$ ) of a zonal wavelength has been compared with the meridional trapping scale. The second perspective may be preferable since the meridional trapping scale is itself only a fraction of a meridional wavelength for the first few meridional modes, and the results below suggest that reanalysis data support this viewpoint.

The need for inclusion of  $2\pi$  in (2.20) can also be anticipated mathematically. The long-wave approximation holds when the quantities in (2.18) are slowly varying in  $x$  and  $t$ , that is, the derivatives of the quantities in (2.18) must satisfy

$$\begin{aligned} |\partial_x \hat{u}(k, y, \omega) \exp[i(\delta_k x - \delta_\omega t)]| \\ \ll |\hat{u}(k, y, \omega) \exp[i(\delta_k x - \delta_\omega t)]|, \end{aligned}$$

for all  $x$  and  $t$  such that the right-hand side is nonzero, with similar relationships for  $\hat{v}$  and  $\hat{\theta}$ . These relationships are identical to the first half of (2.20); similar

constraints on the time derivative of the quantities in (2.18) lead to the second half of (2.20).

Note that the width and height of the region in Fig. 1 associated with (2.21) is proportional to the chosen value of  $\delta_{\max}$ . For example, choosing  $\delta_{\max} = 0.15$  would result in a rectangular region half as wide and half as tall as the region in Fig. 1 (where  $\delta_{\max} = 0.3$ ; i.e., the region would encompass wavenumbers  $|k| \leq 0.65$  and frequencies  $\omega \leq 0.07$  cpd).

### 3. Data and data analysis methods

We now turn to reanalysis data to provide an observation-based estimate of the spatial and temporal scales on which long-wave dynamics occur. NCEP–NCAR reanalysis daily zonal winds, meridional winds, and geopotential height are used to estimate  $u$ ,  $v$ , and  $\theta$ , respectively (Kalnay et al. 1996). These datasets have a horizontal spatial resolution of  $2.5^\circ \times 2.5^\circ$ . The time period used in this study is the 34-yr period from 1 January 1980 to 31 December 2013. The data are made dimensionless by the scales in (2.5) using the parameter values shown in Table 1.

To test the robustness of the results, a second reanalysis dataset with higher resolution was used. All the results presented here were also calculated using the ERA-Interim winds and geopotential during the same time period with  $1^\circ \times 1^\circ$  horizontal resolution and four-times-daily temporal resolution (Dee et al. 2011).

The variable quantities ( $u$ ,  $v$ ,  $\theta$ ) are isolated in the dimensionless data through a series of spectral analysis steps. First, to estimate the first baroclinic component only of each variable, the top and bottom, of the troposphere are associated with the 200- and 850-hPa pressure levels, respectively. When each velocity component is expressed as the sum of the barotropic mode and a first baroclinic mode, the first baroclinic component can be estimated by

$$\begin{aligned} u_{\text{BC}}(x, y, t) &= \frac{u(850 \text{ hPa}) - u(200 \text{ hPa})}{2\sqrt{2}}, \\ v_{\text{BC}}(x, y, t) &= \frac{v(850 \text{ hPa}) - v(200 \text{ hPa})}{2\sqrt{2}}. \end{aligned} \quad (3.1)$$

While temperature data in the middle troposphere could be used as an estimate of  $\theta_{\text{BC}}$ , where

$$\theta(x, y, z, t) = \theta_{\text{BC}}(x, y, t)\sqrt{2}\sin(z), \quad (3.2)$$

here we use geopotential height  $Z$  instead, where

$$Z(x, y, z, t) = Z_{\text{BT}}(x, y, t) + Z_{\text{BC}}(x, y, t)\sqrt{2}\cos(z). \quad (3.3)$$

Similar to (3.1), the first baroclinic component of geopotential height may be estimated by

$$Z_{\text{BC}} = \frac{Z(850 \text{ hPa}) - Z(200 \text{ hPa})}{2\sqrt{2}}. \quad (3.4)$$

Combining hydrostatic balance, that is,

$$\partial Z / \partial p = -\theta, \quad (3.5)$$

with (3.2) and (3.3) results in  $\theta_{\text{BC}} = -Z_{\text{BC}}$ ; substitution of this into (3.4) results in

$$\theta_{\text{BC}}(x, y, t) = -\frac{Z(850 \text{ hPa}) - Z(200 \text{ hPa})}{2\sqrt{2}}. \quad (3.6)$$

Isolation of the first baroclinic mode through this simple vertical projection reduces a 3D ( $x$ ,  $y$ ,  $z$ ) dataset into a 2D ( $x$ ,  $y$ ) dataset.

Next, the dimensionless first baroclinic data are decomposed into their meridional-mode components utilizing the meridional basis functions that take the form of parabolic cylinder functions. Each first baroclinic variable can be expressed as a linear combination of parabolic cylinder functions:

$$u_{\text{BC}}(x, y, t) = \sum_{m=0}^{\infty} u_m(x, t)\phi_m(y), \quad (3.7)$$

where the  $\phi_m(y)$  are the basis functions, the first five of which are

$$\phi_0(y) = \frac{1}{\pi^{1/4}}e^{-y^2/2}, \quad \phi_1(y) = \frac{1}{\pi^{1/4}}\frac{1}{\sqrt{2}}ye^{-y^2/2}, \quad (3.8a)$$

$$\phi_2(y) = \frac{1}{\pi^{1/4}}\frac{1}{2\sqrt{2}}(4y^2 - 2)e^{-y^2/2},$$

$$\phi_3(y) = \frac{1}{\pi^{1/4}}\frac{1}{2\sqrt{12}}(8y^3 - 12y)e^{-y^2/2}, \quad (3.8b)$$

$$\phi_4(y) = \frac{1}{\pi^{1/4}}\frac{1}{4\sqrt{24}}(16y^4 - 48y^2 + 12)e^{-y^2/2}, \quad (3.8c)$$

and are shown in Fig. 2. The spectral coefficients  $u_m(x, t)$  can be approximated by evaluating the integral:

$$u_m(x, t) = \int_{-\infty}^{\infty} u_{\text{BC}}(x, y, t)\phi_m(y) dy. \quad (3.9)$$

Similar formulas apply for  $v$  and  $\theta$ . This meridional projection reduces the 2D ( $x$ ,  $y$ ) dataset to a 1D ( $x$ ) dataset. More details of these projection steps can be found in Stechmann and Majda (2015).

Next, for each spectral coefficient  $u_m$ ,  $v_m$ , and  $\theta_m$ , a seasonal cycle is identified at each longitude  $x$  by the mean and first three annual harmonics. This cycle is then removed at each longitude.

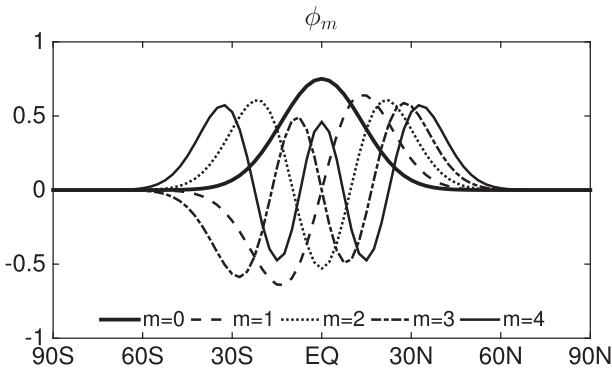


FIG. 2. Meridional basis functions  $\phi_m$  for  $m = 0-4$ .

Finally, the power contained in the anomalies of  $u_m(x, t)$ ,  $v_m(x, t)$ , and  $\theta_m(x, t)$  can then be found through space-time spectral analysis, where the following standard steps are taken here. First, a spatial Fourier transform is taken, and then the data for each wavenumber are partitioned into shorter overlapping time segments. For each segment, the mean is removed and

the first and last 10% of each segment is tapered to zero by a cosine tapering function. Here segments are taken to be 366 days long, with an overlap of 246 days. A temporal Fourier transform of each segment is taken next, and the power in each frequency is estimated by the square of the amplitude of these Fourier coefficients. This power is then averaged over all segments and is denoted throughout the paper by, for example,  $|\hat{u}_m|^2$ ; the logarithm of these quantities can then be displayed in a wavenumber-frequency diagram as in Wheeler and Kiladis (1999).

#### 4. Primitive variables

We now turn to reanalysis data to assess the range of spatial and temporal scales on which long-wave dynamics occur in nature. These scales are quantified first from the perspective of the primitive variables ( $u, v, \theta$ ).

##### Observational data analysis

Figure 3 shows a Hovmöller plot of the zeroth meridional mode of horizontal wind and potential temperature

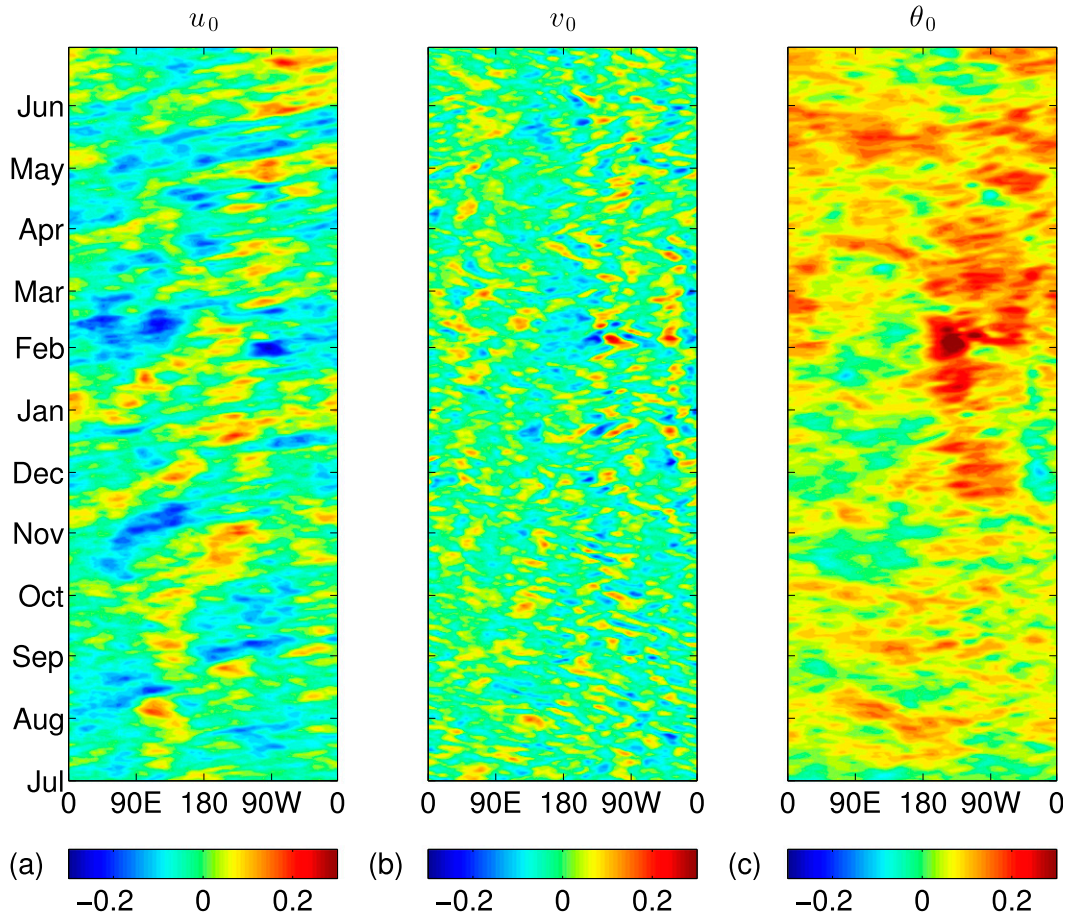


FIG. 3. Hovmöller plots of dimensionless (a)  $u_0$ , (b)  $v_0$ , and (c)  $\theta_0$  anomalies from a seasonal cycle. The time period shown is 1 Jul 2009–30 Jun 2010.

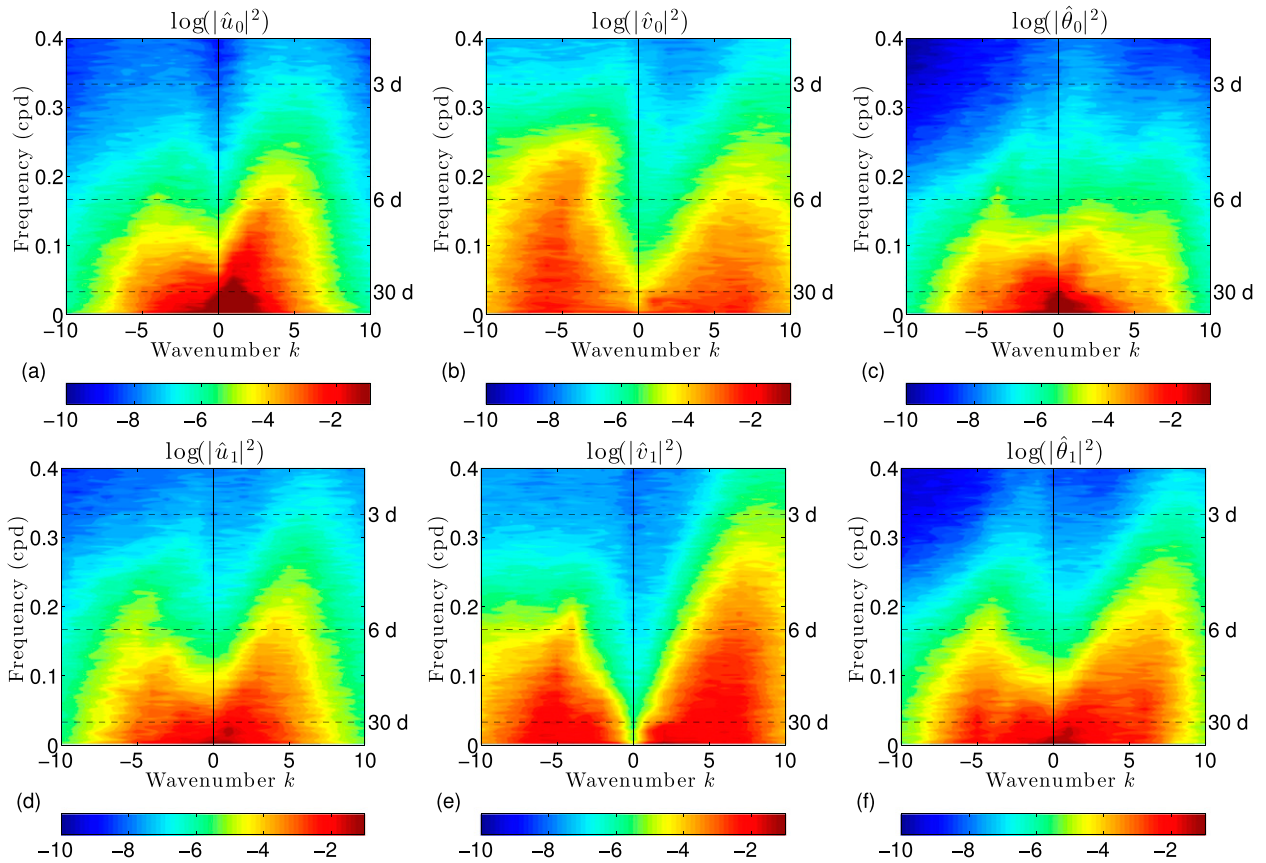


FIG. 4. (a)–(c) Power spectrum of the zeroth meridional mode of the first baroclinic dimensionless (a) zonal wind, (b) meridional wind, and (c) potential temperature anomalies during 1 Jan 1980–31 Dec 2013. Anomalies are from a seasonal cycle. (d)–(f) As in (a)–(c), but for the first meridional mode.

anomalies from a seasonal cycle for the 1-yr period from 1 July 2009 to 30 June 2010. The zonal winds contain evidence of Kelvin waves, seen in the rapid eastward propagation of anomalies throughout the figure. The much slower eastward propagation of anomalies centered between  $90^{\circ}\text{E}$  and  $150^{\circ}\text{W}$  during the months of October 2009–February 2010 are evidence of the well-documented MJO activity during the Year of Tropical Convection (YOTC) (e.g., Moncrieff et al. 2012; Waliser et al. 2012). The meridional wind and potential temperature anomalies exhibit both eastward and westward propagation with the largest anomalies occurring over the Pacific Ocean from approximately  $180^{\circ}$  to  $90^{\circ}\text{W}$ . For both the zonal winds and potential temperature, large anomalies appear to occur primarily on large spatial and temporal scales. In contrast, the meridional wind anomalies appear to occur primarily on small spatial and temporal scales.

A power spectrum confirms that meridional winds are indeed weaker than zonal winds for small wavenumber and frequency. Figure 4 shows the power spectrum for the zeroth and first meridional mode of each variable [i.e., the quantities  $\log(|\hat{u}_m|^2)$ ,  $\log(|\hat{v}_m|^2)$ , and  $\log(|\hat{\theta}_m|^2)$ ,

for  $m = 0, 1$ ]. Consistent with Fig. 3,  $u_0$  contains a majority of power in the eastward direction, while  $v_0$  and  $\theta_0$  show roughly equal power in each direction. For the first meridional mode,  $v_1$  contains considerably more power in the eastward direction, while both  $u_1$  and  $\theta_1$  contain slightly more power in the eastward direction. At low frequencies, both zonal winds and temperature show a significant amount of “red noise” characteristics, while there is a pronounced “double peak” in power spectrum of  $v$  with a trough centered at  $k = 0$ ; both  $|\hat{v}_0|$  and  $|\hat{v}_1|$  contain the most power at low frequencies and moderate wavelengths with  $3 \leq |k| \leq 7$ .

The smallness of  $v$  can be seen more clearly in the ratio of power (i.e.,  $|\hat{v}_m|/|\hat{u}_m|$  and  $|\hat{v}_m|/|\hat{\theta}_m|$ ) shown in Fig. 5 for  $m = 0, 1$ . As expected, these ratios do indeed take on their lowest values at low wavenumbers and frequencies, though the ratio is much smaller than 1 for only a very narrow range of wavenumbers. For example, the solid black contour in Figs. 5a and 5c indicates where  $|\hat{v}_m|/|\hat{u}_m| = 0.3$ , and the solid black contour in Figs. 5b and 5d indicates where  $|\hat{v}_m|/|\hat{\theta}_m| = 0.3$ . This contour lies within the range  $|k| \leq 2$  in Fig. 5a and within the range

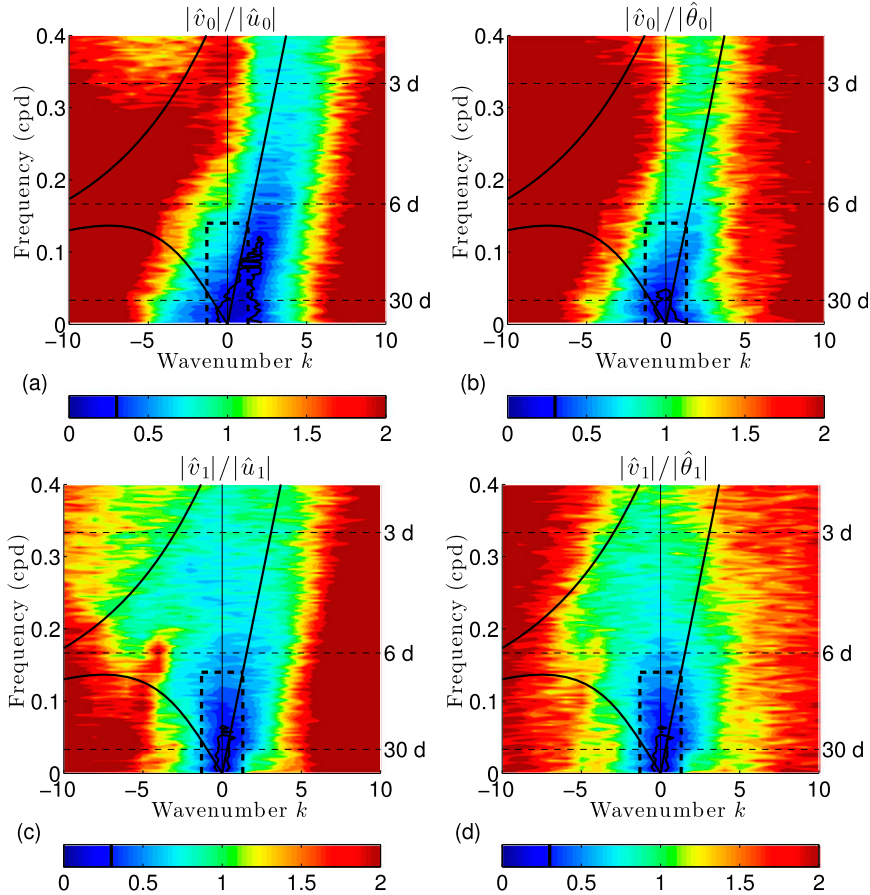


FIG. 5. (a),(c) Power spectrum ratios  $|\hat{v}_m(k, \omega)|/|\hat{u}_m(k, \omega)|$  for  $m = 0$  and  $1$ , respectively. (b),(d) Power spectrum ratios  $|\hat{v}_m(k, \omega)|/|\hat{\theta}_m(k, \omega)|$  for  $m = 0$  and  $1$ , respectively. The dashed black rectangle outlines the region where conditions (2.21) are satisfied with  $\delta_{\max} = 0.3$ ; the solid black curve denotes the 0.3 contour. The dispersion relations for solutions to (2.7) are also shown.

$|k| \leq 1$  in Figs. 5b–d. Note that in all figures displaying the ratio of power in one variable to power in another, the ratio is of the amplitude of the Fourier coefficients (e.g.,  $|\hat{v}_m|/|\hat{u}_m|$ ), not the ratio of the logarithms of the amplitudes.

The spatiotemporal scales that satisfy condition (2.21) are also indicated on each plot by the thick dashed rectangular box. The dark line depicting the 0.3 contour lies entirely within the box in Figs. 5b–d, while a portion lies outside the box in Fig. 5a along a Kelvin wave–type dispersion curve. This box region corresponding to condition (2.21) thus appears in general to slightly overestimate the region where the long-wave approximation holds, but the agreement is reasonable. This slight overestimation persists over a range of values for  $\delta_{\max}$ , including up to  $\delta_{\max} = 0.5$  (not shown).

### 5. Characteristic variables

The results in section 4 suggest that one aspect of the long-wave approximation, small meridional winds, holds

only over a very narrow range of scales. We next examine the data from the perspective of characteristic variables. The equations expressed using characteristic variables are first summarized in sections 5a and 5b; observational analysis results are given in section 5c.

#### a. Definition of characteristic variables

System (2.7) can be expressed succinctly using characteristic variables and ladder operators,

$$r = \frac{1}{\sqrt{2}}(u - \theta), \quad l = \frac{1}{\sqrt{2}}(u + \theta),$$

$$L_{\pm} = \frac{1}{\sqrt{2}}(\partial_y \pm y), \tag{5.1a}$$

$$S_r = \frac{1}{\sqrt{2}}(S_u + S_{\theta}), \quad S_l = \frac{1}{\sqrt{2}}(S_u - S_{\theta}), \tag{5.1b}$$

where the variable names  $r$  and  $l$  are used to suggest “right moving” (i.e., eastward) and “left moving” (i.e.,

westward) quantities. Substitution of (5.1) into (2.7) (i.e., where  $\delta = 1$ ), results in

$$\partial_t r + \partial_x r + L_- v = S_r, \quad (5.2a)$$

$$\partial_t l - \partial_x l - L_+ v = S_l, \quad (5.2b)$$

$$\partial_t v + L_+ r - L_- l = S_v. \quad (5.2c)$$

The quantities ( $r, l, v$ ) and their corresponding source terms  $S_r, S_l$ , and  $S_v$  can be decomposed into their meridional mode components:

$$\begin{pmatrix} r \\ l \\ v \end{pmatrix} (x, y, t) = \sum_{m=0}^{\infty} \begin{pmatrix} r_m \\ l_m \\ v_m \end{pmatrix} (x, t) \phi_m(y). \quad (5.3)$$

Substitution of (5.3) into (5.2) and projection of the result onto each meridional basis function  $\phi_m$  results in a single PDE governing  $r_0$ ,

$$\partial_t r_0 + \partial_x r_0 = S_{r_0}; \quad (5.4)$$

the equations governing the evolution of  $r_1$  and  $v_0$  are

$$\partial_t r_1 + \partial_x r_1 - v_0 = S_{r_1}, \quad (5.5a)$$

$$\partial_t v_0 + r_1 = S_{v_0}; \quad (5.5b)$$

and the evolution of the triplet ( $r_{m+1}, l_{m-1}, v_m$ ) is governed by

$$\partial_t r_{m+1} + \partial_x r_{m+1} - \sqrt{m+1} v_m = S_{r_{m+1}}, \quad (5.6a)$$

$$\partial_t l_{m-1} - \partial_x l_{m-1} - \sqrt{m} v_m = S_{l_{m-1}}, \quad (5.6b)$$

$$\partial_t v_m + \sqrt{m+1} r_{m+1} + \sqrt{m} l_{m-1} = S_{v_m}. \quad (5.6c)$$

### b. Long-wave theory with characteristic variables

Substitution of (5.1) into (2.12) results in

$$\partial_t r + \partial_x r + L_- v' = S_r, \quad (5.7a)$$

$$\partial_t l - \partial_x l - L_+ v' = S_l, \quad (5.7b)$$

$$\delta^2 \partial_t v' + L_+ r - L_- l = \delta S_v. \quad (5.7c)$$

The commonly used form of the long-wave equations are again found by retaining the terms of (5.7) at leading order in  $\delta$ :

$$\partial_t r + \partial_x r + L_- v' = S_r, \quad (5.8a)$$

$$\partial_t l - \partial_x l - L_+ v' = S_l, \quad (5.8b)$$

$$L_+ r - L_- l = 0. \quad (5.8c)$$

The quantity

$$\text{MGI} = L_+ r - L_- l \quad (5.9)$$

in (5.8c) can be described as a measure of geostrophic imbalance in the meridional direction [i.e., meridional geostrophic imbalance (MGI); see Remmel and Smith (2009) for a discussion of similar quantities that measure geostrophic imbalance in the midlatitudes]. Substitution of (5.3) into (5.8) and projection of the result onto  $\phi_0$  results in (5.4); the long-wave version of (5.5) is

$$v_0 = -S_{r_1} \quad (5.10a)$$

$$r_1 = 0; \quad (5.10b)$$

and the long-wave version of (5.6) is two coupled PDEs with a constraint equation governing the evolution of the triplet ( $r_{m+1}, l_{m-1}, v_m$ ):

$$\partial_t r_{m+1} + \partial_x r_{m+1} - \sqrt{m+1} v_m = S_{r_{m+1}}, \quad (5.11a)$$

$$\partial_t l_{m-1} - \partial_x l_{m-1} - \sqrt{m} v_m = S_{l_{m-1}}, \quad (5.11b)$$

$$\sqrt{m+1} r_{m+1} + \sqrt{m} l_{m-1} = 0. \quad (5.11c)$$

### c. Observational data analysis

Turning again to reanalysis data, we first briefly examine the spatiotemporal scales on which  $v$  is small from this viewpoint of characteristic variables. Figure 6 shows the ratios of each quantity  $|\hat{v}_m|/|\hat{r}_{m+1}|$  and  $|\hat{v}_m|/|\hat{l}_{m-1}|$  for  $m = 1-3$ . As in Fig. 5, the solid black line indicates the 0.3 contour. Comparing  $v_m$  with the other components of the triplet ( $r_{m+1}, l_{m-1}, v_m$ ) results in contours with remarkable symmetry about  $k = 0$ ; the corresponding regions in Fig. 5a exhibit less symmetry.

Another feature readily apparent in Fig. 6 is the expanding region of small ratio with increasing meridional mode number  $m$ . This can be qualitatively anticipated from the following physical considerations. As  $m$  increases, the average distance between one local maximum and an adjacent local minimum in the basis function  $\phi_m(y)$  decreases as can be seen in Fig. 2. Thus, it may be expected that the effective meridional length scale is a function of the  $m$ , just as the effective zonal length scale was estimated as a function of wavenumber  $k$  in section 2. The dimensionless distance  $d_m$  from a local maximum nearest the equator to a local minimum nearest the equator for mode  $\phi_m(y)$  is approximately  $d_1 \approx 2.02$  for  $m = 1$ ,  $d_2 \approx 1.58$  for  $m = 2$ , and  $d_3 \approx 1.23$  for  $m = 3$ . For  $m = 0$ , there is no local minimum; one estimate for a distance  $d_0$  analogous to  $d_1, d_2, \dots$  can be found by noting that the distance from the maximum of

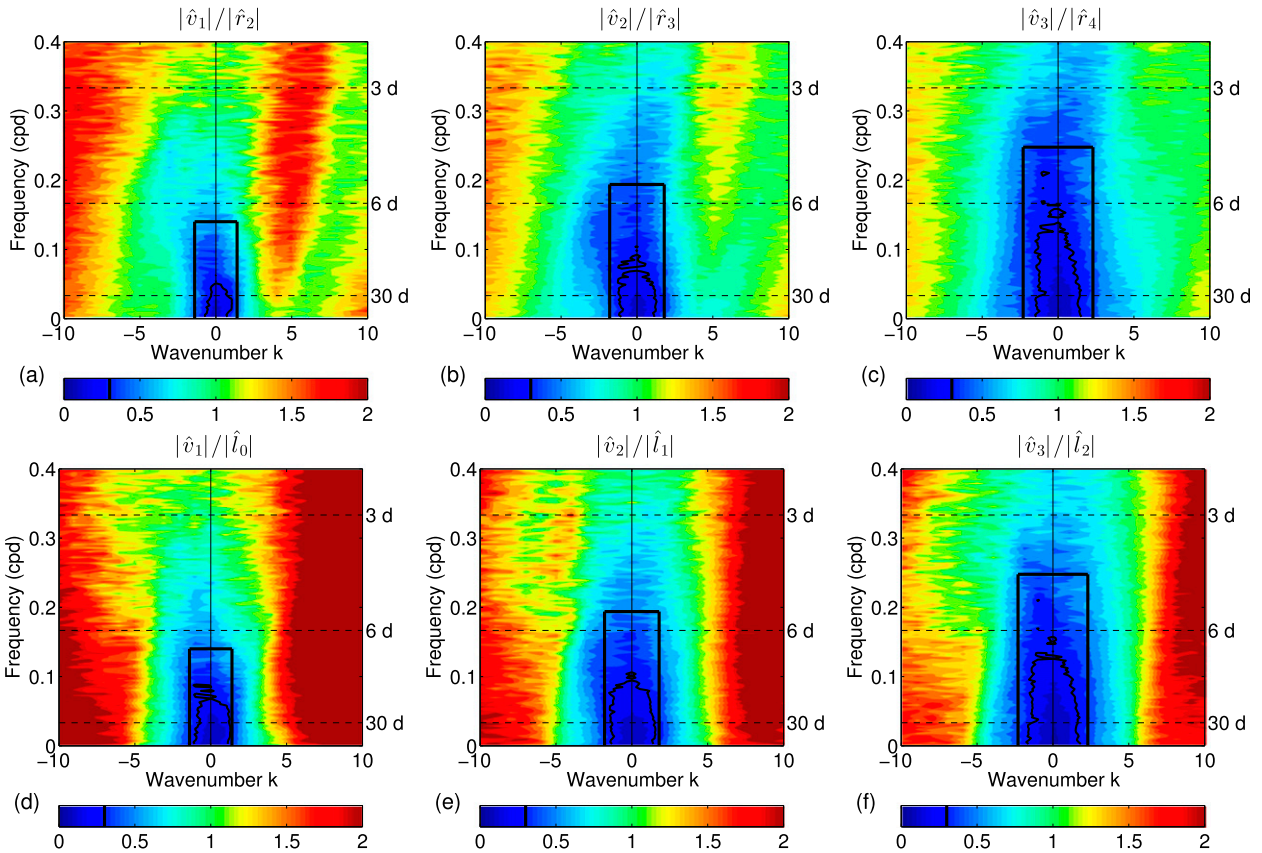


FIG. 6. (a)–(c) Power spectrum ratios  $|\hat{v}_m(k, \omega)|/|\hat{r}_{m+1}(k, \omega)|$  for  $m = 1$ – $3$ , respectively. (d)–(f) Power spectrum ratios  $|\hat{v}_m(k, \omega)|/|\hat{l}_{m-1}(k, \omega)|$  for  $m = 1$ – $3$ , respectively. In (a),(d), the solid black rectangle outlines the region where conditions (2.21) are satisfied with  $\delta_{\max} = 0.3$ ; in (b),(c),(e),(f), this region has been widened by a factor of  $d_0/d_m$  with  $d_0 = 2.15$ ,  $d_1 = 2.02$ ,  $d_2 = 1.58$ , and  $d_3 = 1.23$ . The solid black curve denotes the 0.3 contour.

$\phi_0(y)$  to one-tenth of the maximum is  $d_0 \approx 2.15$ .<sup>2</sup> The wavenumber and frequency ranges found using conditions (2.21) may then be multiplied by a factor of  $d_0/d_m$  for a more detailed estimate of the long-wave scales for each individual meridional mode  $m = 1, 2, 3, \dots$ <sup>3</sup> These adjusted predictions of long-wave scales are depicted by the rectangular boxes in Fig. 6. Despite the crude method used here, the rate of expansion in the predicted

range is in reasonable agreement with the data. We note that the dimensionless distances  $d_m$  are independent of the equivalent depth, or meridional length scale; thus, the ratios  $d_0/d_m$  are also independent of the equivalent depth. We also note that use of an alternate estimate of  $d_0$  (e.g.,  $d_0 = 2$ , not shown), does not have a significant impact on the results.

Before continuing on, we note that one might expect the opposite trend of that seen in Fig. 6 (i.e., one might expect that the region of long-wave scales should shrink with increasing  $m$ ). This expectation could arise by considering that meridional modes of higher number have a wider base of support (i.e., these modes extend farther away from the equator). Thus, it might be expected that higher meridional modes have a larger length scale, which would suggest that the long-wave approximation should only hold over a narrower region of zonal length scales. However, as discussed in the previous paragraph, it is also the case that the distance between peaks in these meridional basis functions decreases with increasing meridional mode number. If this

<sup>2</sup>This method for measuring the width of a Gaussian is one standard approach, although others could certainly be used as well. For example, if the half-width of the Gaussian is estimated by two standard deviations, the result is  $d_0 = 2$ .

<sup>3</sup>The meridional trapping scale is one standard deviation of the Gaussian on which the parabolic cylinder functions are based, and not a full wavelength in the meridional direction. Thus, an argument could be made that a more appropriate estimate could be constructed by requiring that the ratio of one zonal wavelength to one meridional wavelength be small. (Note that this notation “meridional wavelength” is not well defined without further clarification since the distance from one crest to an adjacent crest is not uniform within a given meridional basis function.)

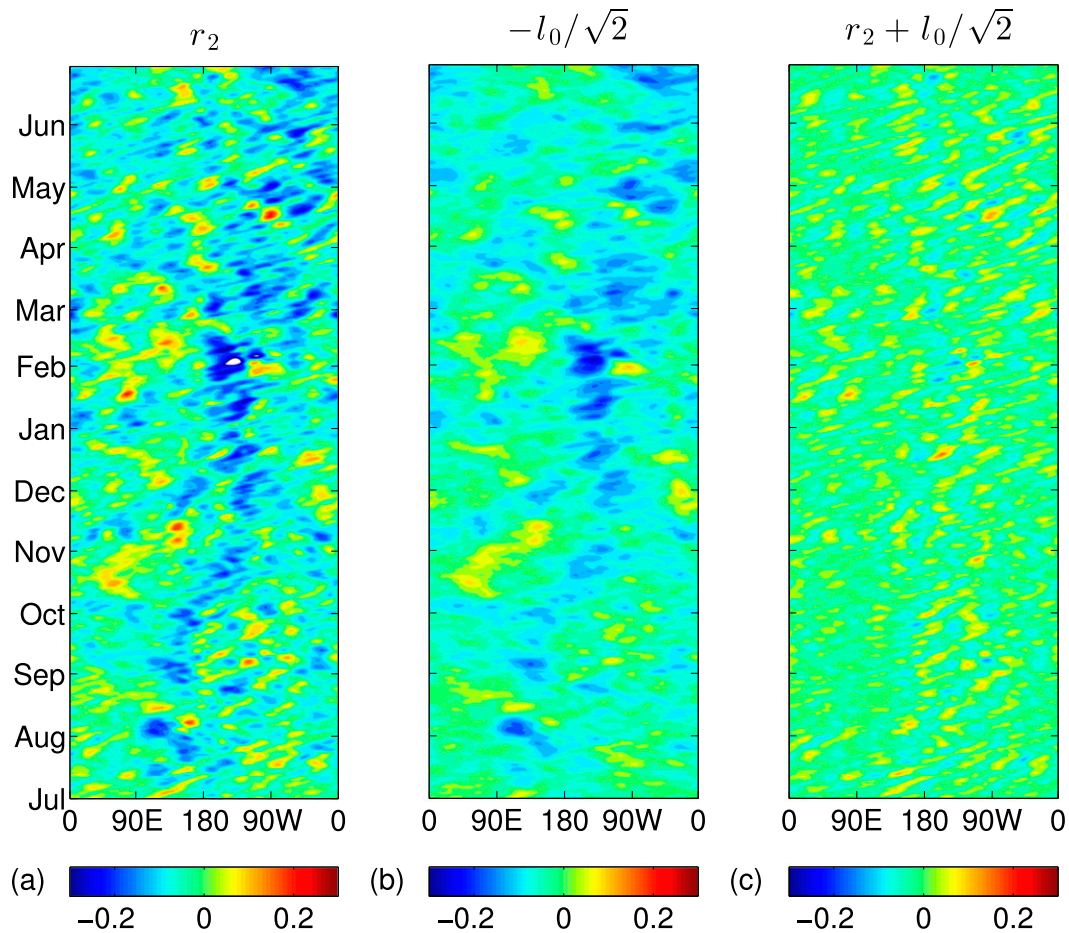


FIG. 7. Hovmöller plots of (a)  $r_2$ , (b)  $-l_0\sqrt{2}$ , and (c)  $\text{MGI}_1 = r_2 + l_0/\sqrt{2}$  anomalies from a seasonal cycle. The time period shown is 1 Jul 2009–30 Jun 2010.

distance between peaks is taken as a meridional length scale  $y_{\text{ref}}$  and the smallest zonal length scale that will satisfy the long-wave approximation is denoted by  $x_{\text{min}}$ , then (2.14) implies that  $x_{\text{min}} \sim y_{\text{ref}}/\delta$  for fixed  $\delta$ . Thus, smaller  $y_{\text{ref}}$  implies smaller  $x_{\text{min}}$  and, hence, larger maximum wavenumber  $k_{\text{max}}$ . The qualitative agreement with the data in Fig. 6 suggests that this viewpoint is indeed justified.

Next we assess the scales on which the data are in meridional geostrophic balance. For an atmosphere in perfect meridional geostrophic balance, the terms  $r_{m+1}$  and  $-\sqrt{m}l_{m-1}/\sqrt{m+1}$  in (5.11c) will be identical for each  $m = 1, 2, \dots$ . Hovmöller plots of these two quantities are shown for  $m = 1$  in Figs. 7a and 7b for a 1-yr period. While there are significant differences between the two quantities, the large-scale features of the two appear to be in good agreement. The difference between these quantities,

$$\text{MGI}_m = r_{m+1} + \frac{\sqrt{m}}{\sqrt{m+1}}l_{m-1}, \quad (5.12)$$

with  $m = 1$ , is shown in Fig. 7c and exhibits anomalies with much smaller amplitude than either original quantity. These differences also appear to occur primarily on small spatial and temporal scales.

This approximate geostrophic balance is confirmed quantitatively, scale by scale, by examining the power spectrum of the quantity  $\text{MGI}_m$ , shown in Figs. 8a–c for  $m = 1–3$ , respectively. In all three panels, the power present in wavenumbers  $-3 \leq k \leq 3$  is dwarfed by the power in wavenumbers  $4 \leq |k| \leq 8$ , consistent with the small scales observed in Fig. 7c. There is also a dominance of eastward propagation that increases with increasing  $m$ ; this may be due to a number of possible factors, including the larger  $\theta$  gradients occurring at latitudes outside of the tropics, which are included in the base of support for higher meridional modes.

Another way to assess the degree of the imbalance term  $\text{MGI}_m$  is to compare its magnitude with that of  $r_{m+1}$ ; the ratio  $|\widehat{\text{MGI}}_m|/|\widehat{r}_{m+1}|$  is shown in Figs. 8d–f. In all three panels, this ratio is small for wavenumbers

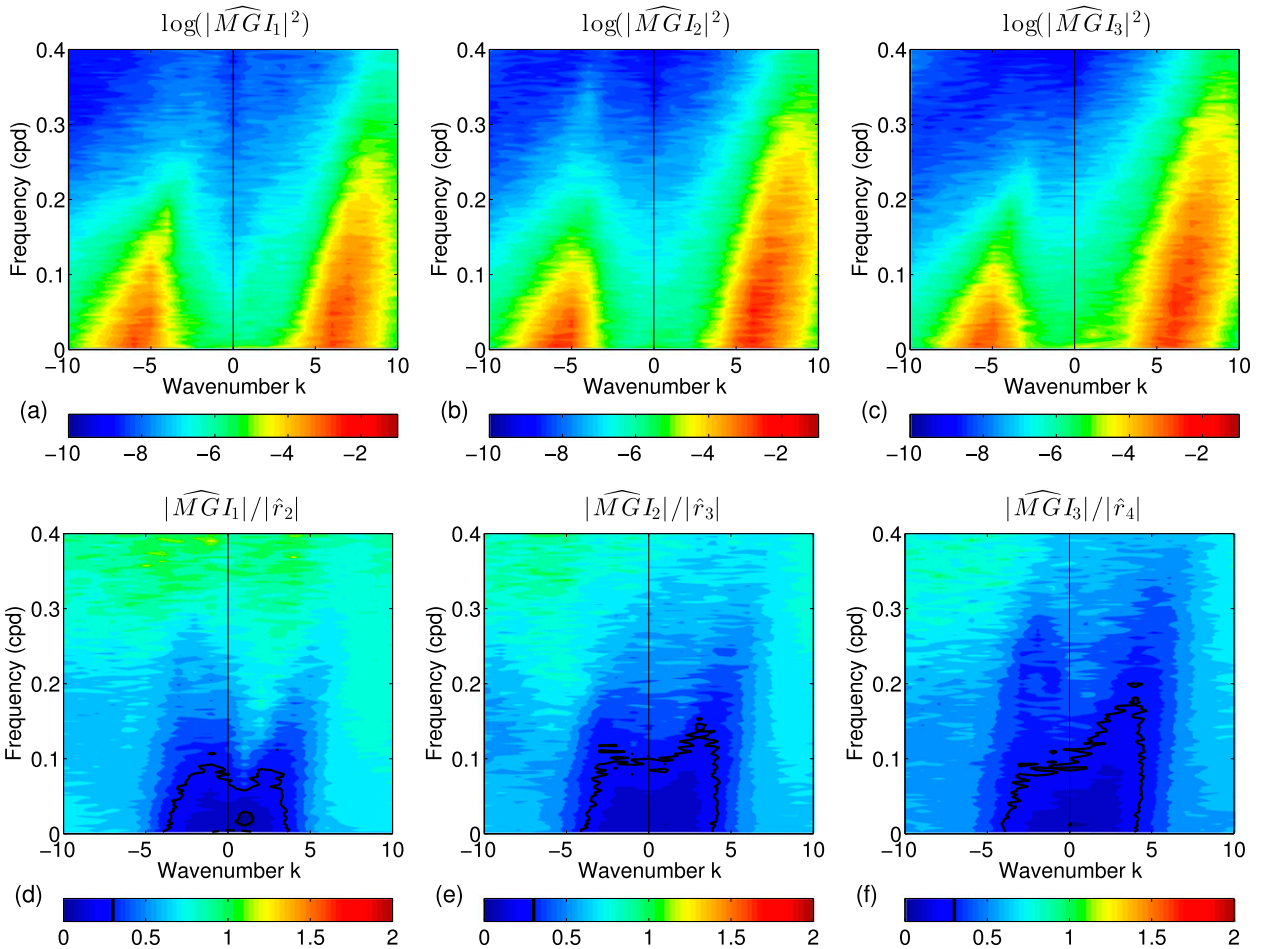


FIG. 8. (a)–(c) Power spectrum of  $MGI_m$  anomalies during 1 Jan 1980–31 Dec 2013 for  $m = 1–3$ , respectively. (d)–(f) Power spectrum ratios  $|MGI_m|/|\hat{r}_{m+1}|$  for  $m = 1–3$ , respectively. The solid black curve denotes the 0.3 contour.

satisfying  $-3 \leq k \leq 3$  and frequencies smaller than 0.1 cpd. This region also expands with increasing  $m$ , particularly in the eastward direction.

An average of the low-frequency power seen in Figs. 8a–c is shown in Fig. 9a, where the quantity

$$\log \left[ \frac{1}{\tilde{\omega}} \int_{\omega=0}^{\omega=\tilde{\omega}} |\widehat{MGI}_m(k, \omega)|^2 \right]^{1/2}, \quad (5.13)$$

is plotted as a function of wavenumber  $k$ , and where an upper frequency cutoff of  $\tilde{\omega}/T_E = 0.25$  cpd has been

used. This low-frequency power is shown for  $m = 1–6$ . For small  $m$ , say  $m \leq 3$ , the power contained in  $|k| \leq 3$  is dwarfed by the power in  $4 \leq |k| \leq 8$ . This trough centered at  $k = 0$  becomes less pronounced as  $m$  increases.

Note that for  $|k| \geq 10$ , the low-frequency power of  $MGI_m$  is smaller than for  $|k| \leq 3$ ; one might conclude that meridional geostrophic balance is better observed at small scales. However, a better measure for the degree of imbalance is perhaps the ratio of the low-frequency power of  $MGI_m$  to the low-frequency power of  $r_{m+1}$ , that is, the relative meridional geostrophic imbalance (RMGI):

$$RMGI_m(k) = \left[ \frac{1}{\tilde{\omega}} \int_{\omega=0}^{\omega=\tilde{\omega}} |\widehat{MGI}_m(k, \omega)|^2 \right]^{1/2} / \left[ \frac{1}{\tilde{\omega}} \int_{\omega=0}^{\omega=\tilde{\omega}} |\hat{r}_{m+1}(k, \omega)|^2 \right]^{1/2}. \quad (5.14)$$

This quantity is shown in Fig. 9b, where (5.14) is plotted as a function of  $k$ . For all  $m$ , this relative

imbalance increases approximately monotonically with increasing  $|k|$ .

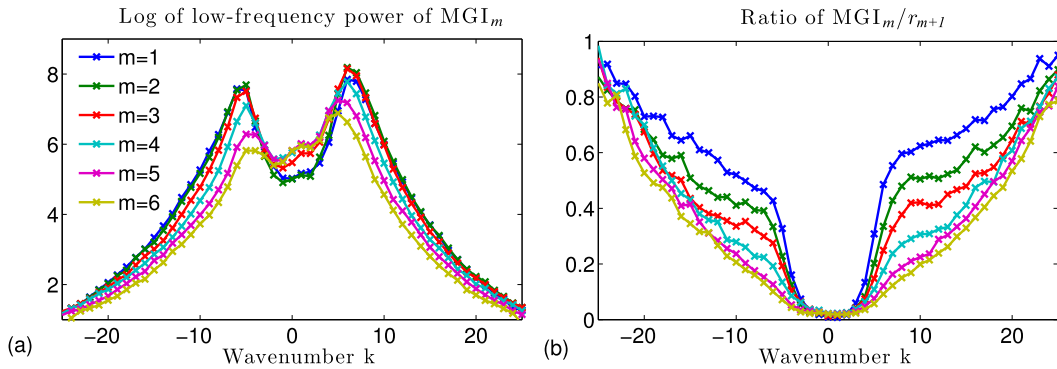


FIG. 9. (a) The log of the average low-frequency power of meridional geostrophic imbalance (MGI) as defined in (5.13) with  $\tilde{\omega}/T_E = 0.25$  cpd for  $m = 1-6$ . (b) The ratio of the average low-frequency power in MGI<sub>*m*</sub> and  $r_{m+1}$  as defined in (5.14) with  $\tilde{\omega}/T_E = 0.25$  cpd for  $m = 1-6$ .

**6. Wave variables**

The results in section 5 suggest that the second aspect of long-wave dynamics considered here (meridional geostrophic balance) is seen in the data over a slightly larger range of spatiotemporal scales than the first aspect (weak meridional winds). The long-wave approximation is next examined from a third viewpoint: wave variables. These wave variables are defined in section 6a, their behavior in the long-wave limit is discussed in section 6b, and their structure is isolated in reanalysis data in section 6c.

*a. Definition of wave variables*

Equations (5.4) and (5.5) describe the evolution of the Kelvin wave, and mixed Rossby–gravity (MRG) and inertio-gravity (EIG<sub>0</sub>) waves, respectively. Equations (5.6) for  $m = 1, 2, \dots$  describe the evolution of the *m*th equatorial Rossby wave  $R_m$  and inertio-gravity waves EIG<sub>*m*</sub> and WIG<sub>*m*</sub>. We focus here on the latter system; analogous results for systems (5.4) and (5.5) are given at the end of this section and in the supplementary material.

Equations (5.6) may be rewritten in terms of these wave variables as follows. Each of the variables and source terms in (5.6) can be expressed as a superposition of plane-wave ansatzes:

$$\begin{aligned} \hat{r}_{m+1}(k, \omega)e^{i(kx-\omega t)}, \quad \hat{l}_{m-1}(k, \omega)e^{i(kx-\omega t)}, \\ \hat{v}_m(k, \omega)e^{i(kx-\omega t)}; \end{aligned} \tag{6.1}$$

substituting (6.1) into (5.6) results in

$$\begin{bmatrix} i(k-\omega) & 0 & -\sqrt{m+1} \\ 0 & -i(k+\omega) & -\sqrt{m} \\ \sqrt{m+1} & \sqrt{m} & -i\omega \end{bmatrix} \begin{pmatrix} \hat{r}_{m+1} \\ \hat{l}_{m-1} \\ \hat{v}_m \end{pmatrix} = \begin{pmatrix} \hat{S}_{r_{m+1}} \\ \hat{S}_{l_{m-1}} \\ \hat{S}_{v_m} \end{pmatrix}. \tag{6.2}$$

We are interested in finding the eigenmodes of the linear operator corresponding to (6.2); its characteristic equation is

$$\omega^3 - (k^2 + 2m + 1)\omega - k = 0. \tag{6.3}$$

There are three solutions  $\omega_j$  for  $j \in \{R_m, \text{EIG}_m, \text{WIG}_m\}$  to (6.3). Each eigenvalue  $\omega_j$  is associated with an eigenvector of the following form:

$$\hat{\mathbf{e}}_j = \left( -\frac{i\sqrt{m+1}}{k-\omega_j}, \frac{i\sqrt{m}}{k+\omega_j}, 1 \right)^T. \tag{6.4}$$

The eigenvectors resulting from (6.4) are shown as a function of *k* in Fig. 10 for  $m = 1$  after normalization. Since the matrix in (6.2) is skew-Hermitian, these normalized eigenvectors form an orthonormal basis.

A straightforward projection technique will be used to assess the degree to which the spatial structure of each of these three waves is seen in reanalysis data. This technique is similar to that used in Stechmann and Majda (2015) and Ogrosky and Stechmann (2015) to identify the MJO. Each day’s reanalysis data are broken into its Fourier components in *x*, that is,  $[\hat{r}_{m+1}(k), \hat{l}_{m-1}(k), \hat{v}_m(k)]^T$ . Since the eigenvectors form an orthonormal basis, the Rossby wave’s Fourier coefficients may be defined as

$$\hat{R}_m(k) = \hat{\mathbf{e}}_{R_m}^\dagger(k) [\hat{r}_{m+1}(k), \hat{l}_{m-1}(k), \hat{v}_m(k)]^T, \tag{6.5}$$

where the dagger denotes the conjugate transpose; analogous definitions apply for the inertio-gravity modes WIG<sub>*m*</sub> and EIG<sub>*m*</sub>. This spectral data may then be transformed back into physical space through an inverse Fourier transform.

In contrast, many previous studies have identified equatorial waves using the eigenvalues from the linear

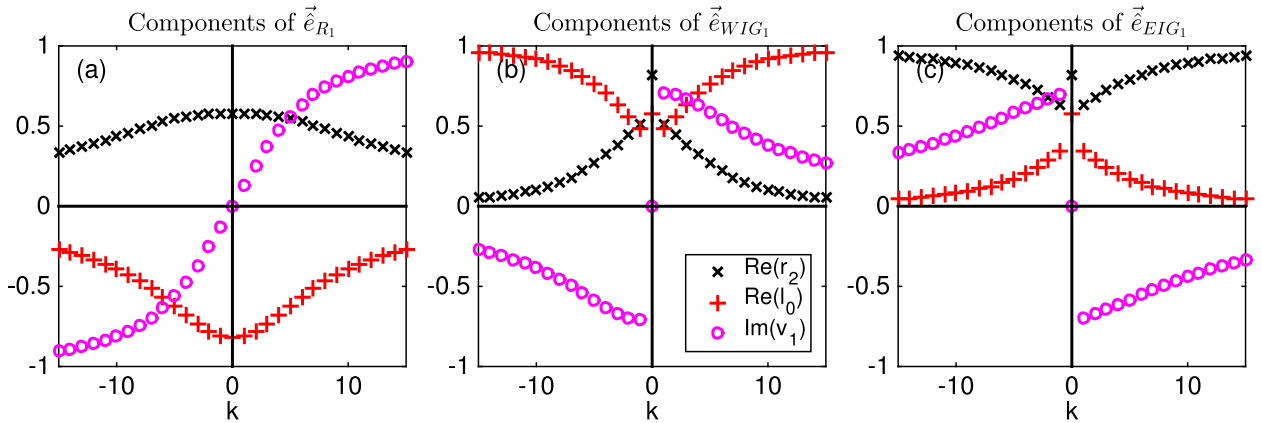


FIG. 10. Components of normalized (a)  $R_1$ , (b)  $WIG_1$ , and (c)  $EIG_1$  eigenvectors as a function of zonal wavenumber  $k$ .

theory. In these studies, space–time filtering of a single variable is used to identify anomalous peaks in its power spectrum. Anomalies that are in close proximity to the eigenvalues  $\omega(k)$  in (6.3) are identified with equatorial waves. Examples include studies by Wheeler and Kiladis (1999) and Dias and Kiladis (2014); the latter study examined regional and seasonal differences in the anomalous peaks in brightness temperature and considered the effect of the background state on the theoretical dispersion curves. Chao et al. (2009) also used space–time filtering and modified the approach of Wheeler and Kiladis to take into account wave structures with both symmetry and asymmetry about the equator. These studies, and others that use this space–time filtering methodology, all define equatorial waves using the eigenvalues from the linear theory.

Other techniques for wave identification have also been used, of which a small sampling is discussed here. A spatial projection technique that made use of spherical harmonics at a single pressure level was used by Madden (2007) to identify free large-scale Rossby waves in the upper troposphere. Matthews and Madden (2000) used Fourier analysis of sea level pressure at nine locations in the tropics to study the 33-h barotropic Kelvin wave; see Salby (1984) for a discussion of earlier observational studies of barotropic equatorial waves. Tindall et al. (2006) used both space–time filtering and a projection technique that does not require selection of an equivalent depth a priori to study the long-term climatology of equatorial waves in the lower stratosphere. Hendon and Wheeler (2008) studied the spatial structure of convectively coupled waves by studying the space–time coherence spectrum of OLR and zonal winds; see Kiladis et al. (2009) for further discussion of the features of convectively coupled waves.

*b. Long-wave theory with wave variables*

We next give a brief summary of the effects of the long-wave approximation on the wave variables. Projecting (5.7) onto  $\phi_{m+1}$  for each  $m = 1, 2, \dots$  results in

$$\partial_t r_{m+1} + \partial_x r_{m+1} - \sqrt{m+1} v'_m = S_{r_{m+1}}, \quad (6.6a)$$

$$\partial_t l_{m-1} - \partial_x l_{m-1} - \sqrt{m} v'_m = S_{l_{m-1}}, \quad (6.6b)$$

$$\delta^2 \partial_t v'_m + \sqrt{m+1} r_{m+1} + \sqrt{m} l_{m-1} = \delta S_{v_m}. \quad (6.6c)$$

In the limit of small  $\delta$ , the system (6.6) can be expressed as an eigenvalue problem (written here in terms of  $\hat{v}_m = \delta \hat{v}'_m$ ):

$$\begin{bmatrix} i\delta(k-\omega) & 0 & -\sqrt{m+1} \\ 0 & -i\delta(k+\omega) & -\sqrt{m} \\ \sqrt{m+1} & \sqrt{m} & -i\delta\omega \end{bmatrix} \begin{pmatrix} \hat{r}_{m+1} \\ \hat{l}_{m-1} \\ \hat{v}_m \end{pmatrix} = \begin{pmatrix} \delta \hat{S}_{r_{m+1}} \\ \delta \hat{S}_{l_{m-1}} \\ \delta \hat{S}_{v_m} \end{pmatrix}. \quad (6.7)$$

The linear operator corresponding to (6.7) has a characteristic equation:

$$\delta^2 \omega^3 - (\delta^2 k^2 + 2m + 1)\omega - k = 0. \quad (6.8)$$

There are again three solutions,  $\omega_j$ , for  $j \in \{R_{LWm}, EIG_{LWm}, WIG_{LWm}\}$  to (6.8); in the limit  $\delta \rightarrow 0$ , the Rossby root  $\omega_{R_{LWm}}$  is a regular root while the inertio-gravity roots  $\omega_{EIG_{LWm}}$  and  $\omega_{WIG_{LWm}}$  are singular. Each eigenvalue  $\omega_j$  is associated with an eigenvector of the following form:

$$\hat{\mathbf{e}}_j = \left( -\frac{i\sqrt{m+1}}{k-\omega_j}, \frac{i\sqrt{m}}{k+\omega_j}, \delta \right)^T. \quad (6.9)$$

In the long-wave limit  $\delta \rightarrow 0$ , approximate eigenvalues may be found by expanding in powers of  $\delta$ :

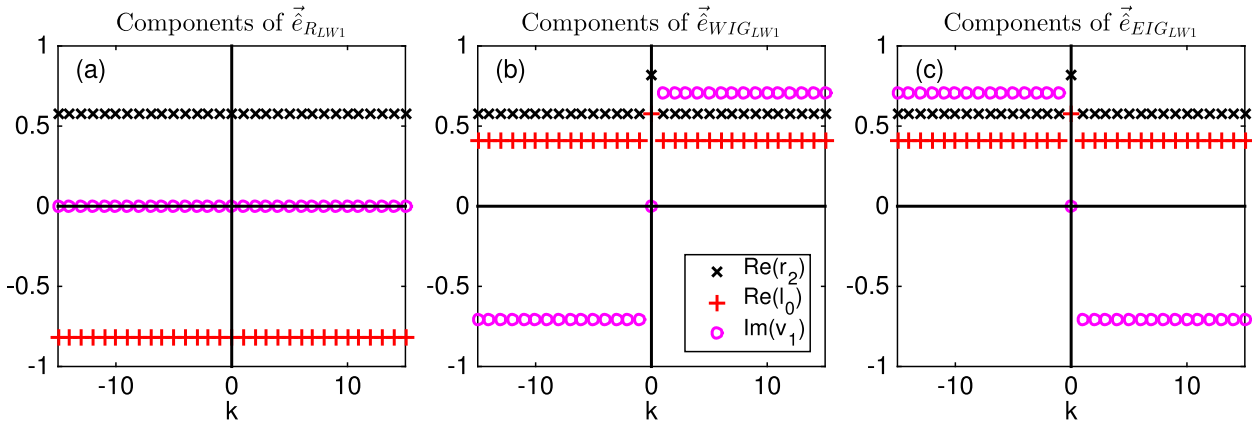


FIG. 11. The normalized long-wave versions of eigenvector components shown in Fig. 10.

$$\omega_{R_{LWm}} = -\frac{k}{2m+1} + O(\delta^2), \tag{6.10a}$$

$$\omega_{WIG_{LWm}} = -\delta^{-1}\sqrt{2m+1} + \frac{k}{2(2m+1)} + O(\delta), \tag{6.10b}$$

$$\omega_{EIG_{LWm}} = \delta^{-1}\sqrt{2m+1} + \frac{k}{2(2m+1)} + O(\delta). \tag{6.10c}$$

After a phase shift so that the  $r_{m+1}$  component is positive and real, these long-wave eigenvectors are, to leading order in  $\delta$ , given by

$$\text{LW Rossby: } \hat{\mathbf{e}}_{R_{LWm}} = \left( \frac{\sqrt{m}}{\sqrt{2m+1}}, -\frac{\sqrt{m+1}}{\sqrt{2m+1}}, 0 \right)^T, \tag{6.11a}$$

$$\text{LW WIG: } \hat{\mathbf{e}}_{WIG_{LWm}} = \left( \frac{\sqrt{m+1}}{\sqrt{4m+2}}, \frac{\sqrt{m}}{\sqrt{4m+2}}, -\frac{i\sqrt{2m+1}}{\sqrt{4m+2}} \right)^T, \tag{6.11b}$$

$$\text{LW EIG: } \hat{\mathbf{e}}_{EIG_{LWm}} = \left( \frac{\sqrt{m+1}}{\sqrt{4m+2}}, \frac{\sqrt{m}}{\sqrt{4m+2}}, \frac{i\sqrt{2m+1}}{\sqrt{4m+2}} \right)^T. \tag{6.11c}$$

The long-wave approximation aids in the identification of waves by offering simpler eigenvector formulas that are independent of wavenumber; these eigenvectors are shown in Fig. 11. The long-wave Rossby structure can then be defined to leading order by<sup>4</sup>

<sup>4</sup>The definition of the long-wave Rossby structure  $\hat{R}_{LWm}$  used here is different than the one used in several previous studies (e.g., Majda and Stechmann 2009; Stechmann and Majda 2015). Here,  $\hat{R}_{LWm}$  has been defined by using the normalized eigenvector  $\hat{\mathbf{e}}_{R_{LWm}}$  in (6.11a). Earlier studies have defined  $\hat{R}_{LWm}$  by analogy with potential vorticity in fluid flow, resulting in  $\hat{\mathbf{e}}_{R_{LWm}} = (\sqrt{m+1}, -\sqrt{m}, 0)^T$ . For data in perfect meridional geostrophic balance, these definitions produce identical Rossby wave structures after normalization.

$$\hat{R}_{LWm}(k) = \hat{\mathbf{e}}_{R_{LWm}}^\dagger(k) [\hat{r}_{m+1}(k), \hat{l}_{m-1}(k), \hat{v}_m(k)]^T. \tag{6.12}$$

The formula for long-wave  $R_m(x, t)$  can also be written explicitly in terms of  $u$  and  $\theta$  in physical space; hence, the wave projection can be performed without the need for Fourier transforms, and the definition of  $R_m(x, t)$  can be more easily understood in terms of the physically intuitive variables  $u$  and  $\theta$  (Stechmann and Majda 2015).

We note that the leading order of the long-wave Rossby eigenvalue in (6.10a) is only expected to be a good approximation of the eigenvalue for small zonal wavenumber  $k$ . This long-wave approximate Rossby eigenvalue is also a feature of other balance models that are based on the equatorial long-wave scaling (Stevens et al. 1990; Chan and Shepherd 2013, 2014). For any wavenumber  $k$ , not necessarily small, the Rossby eigenvalue is approximately  $-k/(2m+1+k^2)$  (e.g., Matsuno 1966; Schubert et al. 2009). Similarly, the long-wave eigenvectors in (6.11) are only expected to be a good approximation of (6.9) when  $k$  is small. Nevertheless, in the observational data analysis below, it will be shown that use of the approximate Rossby structure in (6.11a) produces a projection remarkably similar to the standard Rossby structure.

The amplitudes of the long-wave structures can be studied theoretically by rewriting (6.6) as a diagonal system in terms of the wave variables  $\hat{R}_{LWm}$ ,  $\widehat{WIG}_{LWm}$ , and  $\widehat{EIG}_{LWm}$  and their corresponding source terms:

$$\frac{d}{dt} \hat{R}_{LWm} + i\omega_{R_{LWm}} \hat{R}_{LWm} = \hat{S}_{R_1}, \tag{6.13a}$$

$$\frac{d}{dt} \widehat{WIG}_{LWm} + i\omega_{WIG_{LWm}} \widehat{WIG}_{LWm} = \hat{S}_{WIG_1}, \tag{6.13b}$$

$$\frac{d}{dt} \widehat{EIG}_{LWm} + i\omega_{EIG_{LWm}} \widehat{EIG}_{LWm} = \hat{S}_{EIG_1}. \tag{6.13c}$$

Each of these wave variables and source terms may be expanded in powers of  $\delta$ :

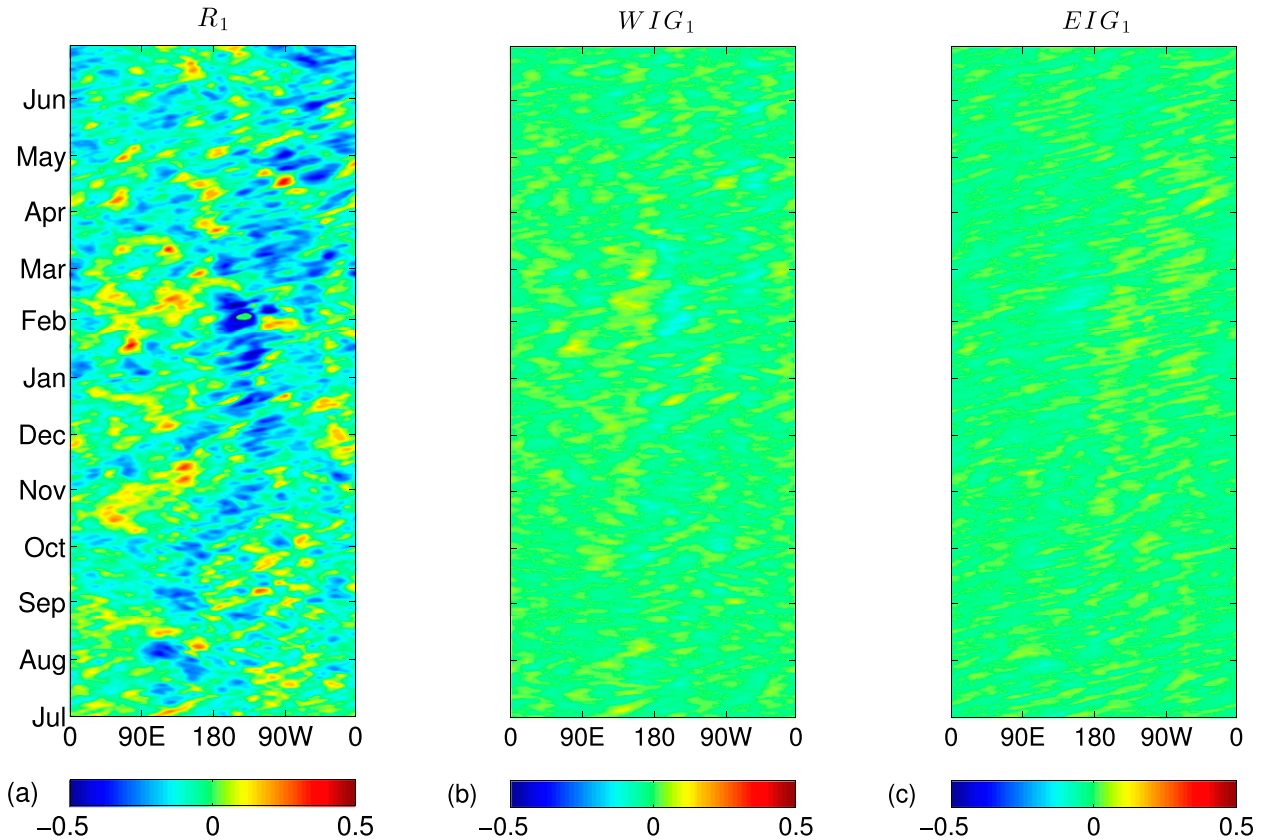


FIG. 12. Hovmöller plot of (a)  $R_1$ , (b)  $WIG_1$ , and (c)  $EIG_1$  anomalies from a seasonal cycle. The time period shown is 1 Jul 2009–30 Jun 2010.

$$\hat{R}_{LWm} = \hat{R}_{LWm}^{(0)} + \delta \hat{R}_{LWm}^{(1)} + O(\delta^2), \quad (6.14a)$$

$$\widehat{WIG}_{LWm} = \widehat{WIG}_{LWm}^{(0)} + \delta \widehat{WIG}_{LWm}^{(1)} + O(\delta^2), \quad (6.14b)$$

$$\widehat{EIG}_{LWm} = \widehat{EIG}_{LWm}^{(0)} + \delta \widehat{EIG}_{LWm}^{(1)} + O(\delta^2). \quad (6.14c)$$

Substituting (6.14) into (6.13) and noting that  $\omega_{R_{LWm}} = O(1)$  and  $\omega_{WIG_{LWm}} = -\omega_{EIG_{LWm}} = O(\delta^{-1})$  results in

$$\frac{d}{dt} \hat{R}_{LWm}^{(0)} + i\omega_{R_{LWm}} \hat{R}_{LWm}^{(0)} = \hat{S}_{R_1}^{(0)}, \quad (6.15a)$$

$$\widehat{WIG}_{LWm}^{(0)} = 0, \quad (6.15b)$$

$$\widehat{EIG}_{LWm}^{(0)} = 0. \quad (6.15c)$$

Thus on long-wave spatiotemporal scales, the Rossby wave structure  $\hat{R}_{LWm}$  evolves at leading order according to (6.15a), while the wave variables  $\widehat{WIG}_{LWm}$  and  $\widehat{EIG}_{LWm}$  are expected to have smaller amplitude. This aspect of the long-wave approximation is sometimes referred to as the “filtering out” of inertio-gravity waves.

c. Observational data analysis

Figure 12 shows a Hovmöller plot of the standard Rossby and inertio-gravity wave structures from (6.9) in

reanalysis data using the projection technique described in section 6a. The most obvious feature is that the inertio-gravity waves clearly have much smaller amplitudes than the Rossby wave. The variability that does exist in the inertio-gravity waves appears to occur primarily on short length and time scales. Also apparent is that the Rossby and westward inertia-gravity (WIG) wave structures each exhibit both periods of eastward and westward propagation, while the eastward inertia-gravity (EIG) wave structure exhibits mostly eastward propagation.

These features are confirmed by the power spectrum of each wave structure, shown in Fig. 13, and deserve additional comment. We note that studies that use space–time filtering to identify free equatorial waves have shown that EIG and WIG waves have less power than Rossby waves, a feature consistent with the redness of the background spectrum. Here, however, the waves are defined solely by their spatial structure; no temporal filtering has been used. While it is reasonable to conjecture that the spatial structures of inertio-gravity waves would contain less power than Rossby waves at low frequencies, it is not clear a priori that this must necessarily be the case with the method employed here.

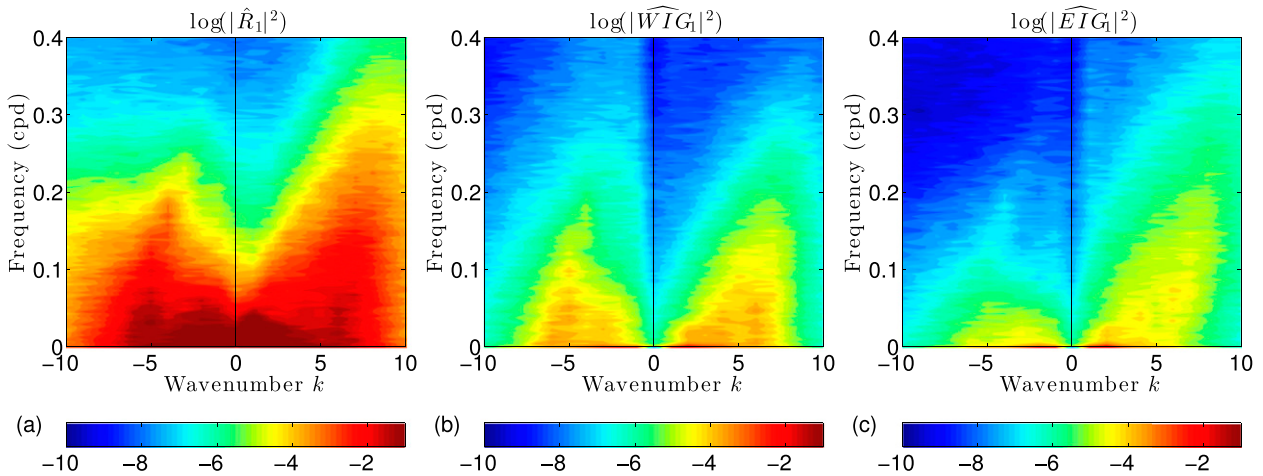


FIG. 13. Power spectrum of (a)  $R_1$ , (b)  $WIG_1$ , and (c)  $EIG_1$  anomalies during 1 Jan 1980–31 Dec 2013.

Also, while free Rossby and WIG waves propagate strictly westward and free EIG waves propagate strictly eastward, the picture is more complicated for forced waves. Nonlinear advection, heating and cooling, dissipation, etc. all can contribute to the forcing terms  $S_u(x, y, t)$ ,  $S_v(x, y, t)$ , and  $S_\theta(x, y, t)$  in (2.4). In nature, these terms contain contributions from many wavenumbers  $k$  and frequencies  $\omega$ , even  $k$  and  $\omega$  that do not lay along the dispersion curves for free waves. In such a case, a forced wave can arise where the structure of, for example, a Rossby wave can propagate eastward if the forcing vector  $(S_u, S_v, S_\theta)$  projects onto the Rossby wave structure so that  $\hat{S}_{R_1} \neq 0$  in (6.13a). In addition, the presence of nontrivial background states in the tropical troposphere have been shown to produce Doppler

shifting of equatorial waves (Dias and Kiladis 2014); see also Yang et al. (2003), who showed that in some regions of the tropics, Rossby waves may propagate eastward.

Figure 14 shows the ratio of power in the inertio-gravity waves  $WIG_1$  and  $EIG_1$  to the Rossby wave  $R_1$ . This ratio is smallest for a region near  $k = 0$  and  $\omega = 0$  but is also small for a large range of wavenumber and frequency. This suggests that over these scales, the three-dimensional data  $(r_2, l_0, v_1)$  can be effectively represented by one-dimensional data  $R_1$ . We note that the spatiotemporal scales at which inertio-gravity waves contain more power than Rossby waves do not necessarily lay along the inertio-gravity wave dispersion curves of the linear theory; note that these curves are not even visible in Fig. 14 as they lay entirely within a higher-frequency range

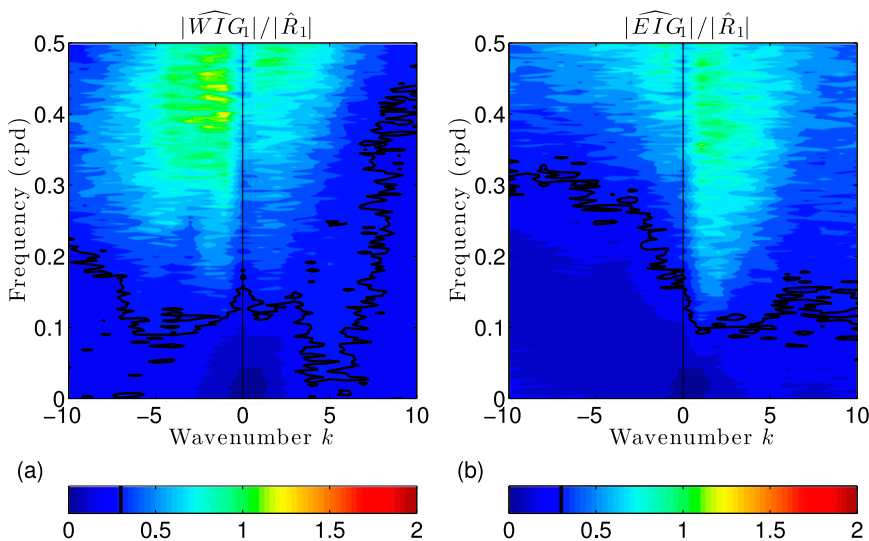


FIG. 14. Power spectrum ratios (a)  $|\widehat{WIG}_1|/|\widehat{R}_1|$  and (b)  $|\widehat{EIG}_1|/|\widehat{R}_1|$ . The solid black curve denotes the 0.3 contour.

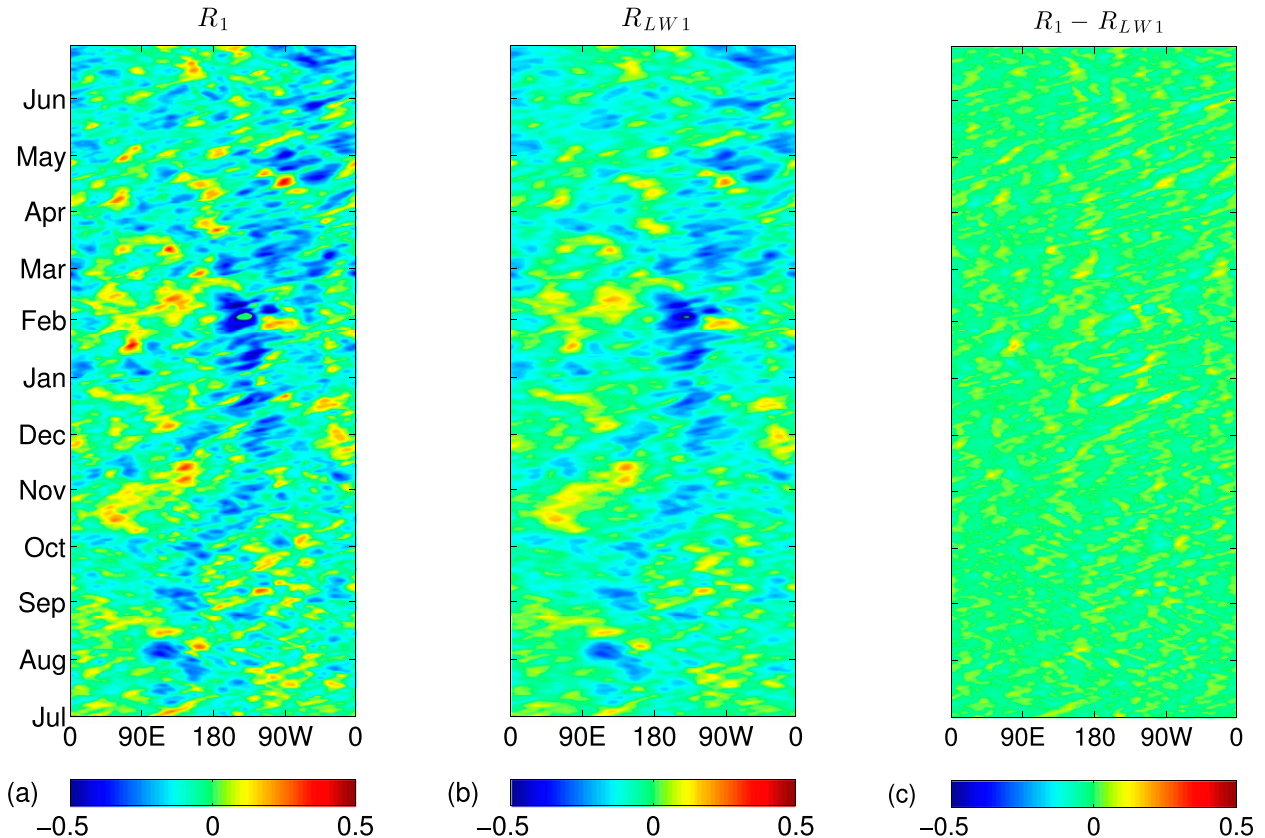


FIG. 15. Hovmöller plot of (a)  $R_1$ , (b)  $R_{LW1}$ , and (c)  $R_1 - R_{LW1}$  anomalies from a seasonal cycle. The time period shown is 1 Jul 2009–30 Jun 2010.

(see Fig. 1). This is likely explained at least in part by the previous discussion of forced waves; that is, the forcing terms in nature contain contributions from many wavenumbers and frequencies, even those that do not lay along the free dispersion curves. Also, at wavenumbers and frequencies that are not near either the inertio-gravity or Rossby dispersion curves, it is unclear a priori which structure will emerge as the dominant one with the spatial projection method used here. However, note that the inertio-gravity waves contain more power than the Rossby structure only at high frequencies (0.3 cpd and higher) with the EIG structure showing greater relative power in the eastward direction and the WIG structure displaying more relative power in the westward direction. Last, the WIG wave structure contains greater power than the EIG wave structure; this is potentially consistent with previous evidence that free WIG waves have been identified more easily than free EIG waves in the troposphere (e.g., Wheeler and Kiladis 1999).

The features of Fig. 14 discussed above are all present in the ERA-Interim data as well (not shown). Use of this higher-resolution dataset does result in a slightly larger ratio of  $WIG_1$  to  $R_1$  power in the westward direction at

frequencies of 0.3–0.5 cpd. Similarly, ERA-Interim data shows a larger ratio of  $EIG_1$  to  $R_1$  in the eastward direction at similar frequencies. The higher inertio-gravity wave power present in high-resolution ERA-Interim data is consistent with other studies of equatorial waves [see, e.g., Tindall et al. (2006) for a discussion of the limitations of using coarse resolution reanalyses for identifying inertio-gravity waves in the lower stratosphere]. However, for the low frequencies of interest in long-wave modeling, use of ERA-Interim data results in ratios that are essentially unchanged from those of Fig. 14.

Given the strength of the Rossby wave relative to the IG waves, it is natural to wonder if a further simplification can be made by using the long-wave form of the Rossby wave  $R_{LW1}$  in (6.12) to approximate the full Rossby wave in reanalysis data. Figures 15a and 15b show a Hovmöller plot for  $R_1$  and  $R_{LW1}$  from 1 July 2009 to 30 June 2010. Most of the large-scale features of the full Rossby wave are also present in the long-wave version, while some of the small-scale features appear to be filtered out. This is confirmed qualitatively by Fig. 15c, which shows a Hovmöller plot of the difference

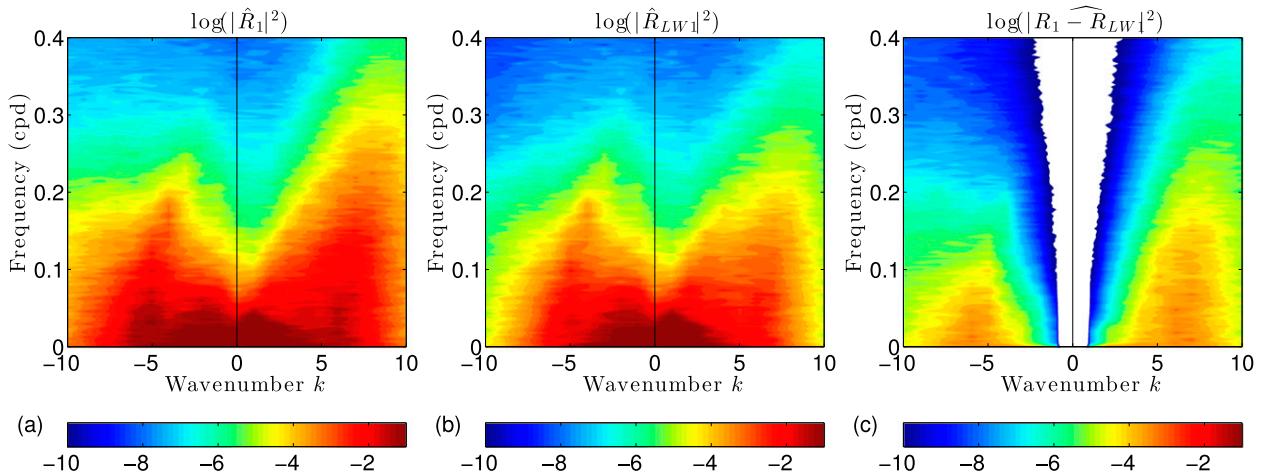


FIG. 16. Power spectrum of (a)  $R_1$ , (b)  $R_{LW1}$ , and (c)  $R_1 - R_{LW1}$  anomalies during 1 Jan 1980–31 Dec 2013.

between the two Rossby structures. The amplitude of the difference is small and there is no discernible low-wavenumber or low-frequency activity. These observations are further confirmed by examining the corresponding power spectra of  $R_1$ ,  $R_{LW1}$ , and the difference between the two, which are shown in Fig. 16. Note the pronounced trough of the difference centered at  $k = 0$ . The results here also suggest that equatorial Rossby waves with zonal wavenumber  $k = 1-4$  should be able to be modeled effectively using long-wave asymptotics.

This analysis was also conducted for the  $\phi_0$  and  $\phi_1$  components of (5.2) corresponding to the Kelvin, MRG, and  $EIG_0$  waves. Figure 17 shows the power spectrum density of the Kelvin, MRG, and  $EIG_0$  anomalies from a seasonal cycle. The Kelvin wave structure has significant power at low frequencies and low wavenumbers, consistent with its important role in long-wave dynamics. On the other hand, the MRG and  $EIG_0$  wave structures

have less spectral power at low frequencies and low wavenumbers, consistent with their absence dynamically from the long-wave theory. Additional results for these waves can be found in the supplementary materials.

In summary, all of these figures demonstrate that reanalysis data projects weakly onto the spatial structures of inertio-gravity waves over a broad range of wavenumbers and frequencies.

## 7. Discussion

We note that there are many other facets of the tropical atmosphere that have been neglected here. For one, the effects of both dissipative mechanisms (e.g., Rayleigh friction and Newtonian cooling) and forcing (e.g., convective heating and radiative cooling) have not been directly quantified here. The results presented,

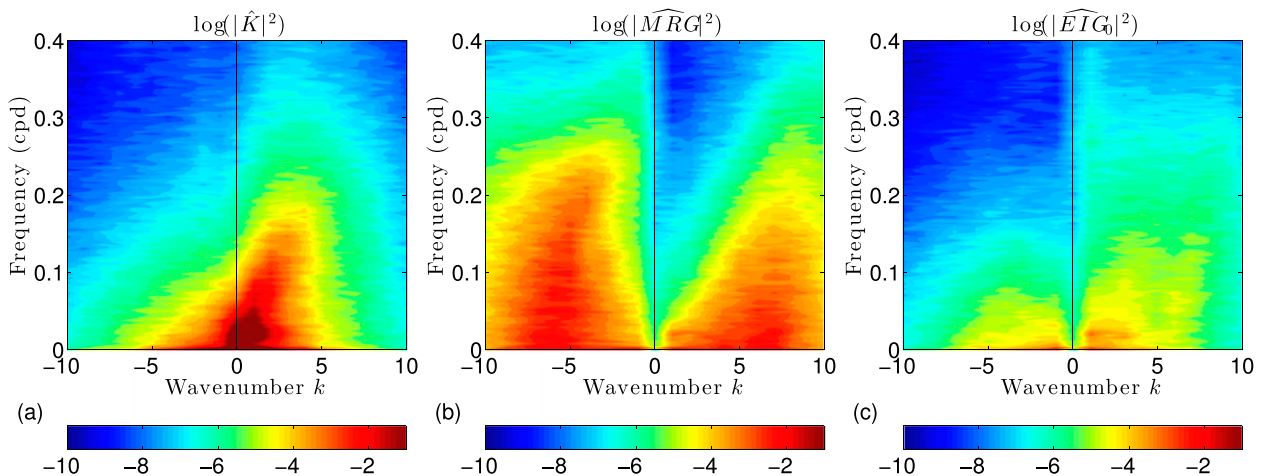


FIG. 17. Power spectrum of the (a) Kelvin, (b) MRG, and (c)  $EIG_0$  wave anomalies during 1 Jan 1980–31 Dec 2013.

however, do contain contributions from both free and forced waves in the tropical troposphere, and the impact of forcing on the results was discussed in section 6. While some aspects of the tropical circulation have been modeled well without the traditional damping terms [e.g., the Walker circulation (Stechmann and Ogrosky 2014) and the MJO (Majda and Stechmann 2009)], both forcing and dissipative mechanisms have been shown to play a significant role in the tropical atmosphere; it would be interesting to directly study the role these mechanisms play in setting the long-wave scales presented here.

In addition, the first baroclinic mode has been studied exclusively here, in part due to the primary role it plays in many models of the tropical atmosphere; it would be interesting to adapt the data analysis methods used here for other vertical modes. The nonlinear interactions between different vertical modes have also been neglected here. Neglecting these nonlinearities allows for the clear spectral methods presented here, but any role these nonlinearities play in setting the long-wave scales has not been considered here [see, e.g., Lin et al. (2005) and Lin et al. (2008) for estimates of the role these nonlinearities play in the tropical atmosphere, and Stechmann et al. (2008) for a model of nonlinear interactions between two baroclinic modes]. The results presented here, however, suggest that when a snapshot of the tropical atmosphere is described in terms of the solutions to Matsuno's linear shallow-water theory, the degree to which each solution is present in the data is in good agreement with the long-wave approximation statistically.

Also, this study has focused solely on the dry variables used in Matsuno (1966); since convectively coupled waves tend to exhibit different scaling than their dry counterparts, it would be interesting to extend this quantitative assessment to include the role of moisture in setting these long-wave scales. Last, the focus here has been on the tropical atmosphere; it would be interesting to adapt this assessment technique to oceanic long-wave dynamics considered in Harvey and Patzert (1976), Legeckis (1977), and Legeckis et al. (1983) or to mid-latitude or global atmospheric dynamics.

## 8. Conclusions

This paper has provided a quantitative assessment of the spatiotemporal scales on which long-wave dynamics are seen in reanalysis data. Specifically, three interconnected aspects of the equatorial long-wave approximation were considered: (i) the smallness of meridional wind anomalies relative to those of zonal winds and potential temperature, (ii) the leading-order dynamics being in meridional geostrophic balance, and (iii) the

filtering out of inertio-gravity waves. This assessment was achieved by using a spectral method that allows for analysis from three different perspectives: primitive variables ( $u, v, \theta$ ), characteristic variables ( $r, l, v$ ), and wave variables (e.g.,  $K$  and  $R_m$ ).

This assessment illustrated that different aspects of long-wave dynamics may exist over different ranges of spatiotemporal scales. Specifically, it was shown that while meridional winds are small for a very narrow range of length scales ( $|k| \lesssim 1$ ) and time scales ( $\omega/T_E \lesssim 0.1$  cpd), dynamics exhibit meridional geostrophic balance and small-amplitude gravity wave structures over a significantly broader range of scales ( $|k| \lesssim 4$ ,  $\omega/T_E \lesssim 0.2$  cpd). Small meridional wind is thus the first feature associated with the long-wave approximation to break down; meridional geostrophic balance and small inertio-gravity wave amplitudes are features of the long-wave approximation that are observed, at least statistically, to hold for a larger range of zonal wavenumbers. As a result, when asking the question "Over what spatiotemporal scales can one expect models employing the long-wave approximation to be valid?," the answer may depend on what implications of the long-wave approximation are of most relevance for a particular model or application.

The results here do suggest that the largest-scale features of the tropical atmosphere (e.g., the Walker circulation and the MJO), whose main features are well described with small zonal wavenumbers, say,  $k = 1-4$ , may be effectively modeled using the long-wave approximation, provided the model and data are compared using a wave perspective [see, e.g., Stechmann and Majda (2015) (MJO) and Stechmann and Ogrosky (2014) (Walker circulation)]. This wave perspective was identified as one of the factors contributing to the good agreement found between a simple model and observations of the Walker circulation in Stechmann and Ogrosky (2014). Of course, even for scales where the tropical atmosphere exhibits long-wave dynamics statistically, the dynamics of the atmosphere at a given moment may not be well described by the long-wave approximation.

Several further issues were also raised and described in more detail in section 7. For example, the present study did not explicitly account for many effects such as nonlinearity, water vapor, convection, and other forcing and dissipative mechanisms. Such effects are major challenges for idealized models and major challenges for comparing theory with observational data. Despite these simplifications, the main characteristics of long-wave dynamics could still be identified here.

An important ongoing task is assessing the accuracy of the many low-dimensional models of the tropical

atmosphere that make use of equatorial long-wave theory (e.g., Majda and Biello 2003; Majda and Stechmann 2009; Stechmann and Ogrosky 2014). Such assessments are typically made by comparing model results with observational or reanalysis data (Stechmann and Ogrosky 2014; Stechmann and Majda 2015; Ogrosky and Stechmann 2015). If significant discrepancies between model and observations exist, it is important to understand whether these discrepancies are due to the long-wave approximation or to some other simplifying assumption (e.g., treatment of convective heating). It is our hope that the quantitative assessment presented here provides an additional resource for such assessments.

*Acknowledgments.* The data for this paper are available from NOAA/OAR/ESRL PSD, Boulder, Colorado, from their website at <http://www.esrl.noaa.gov/psd/>. The research of S.N.S. is partially supported by ONR Young Investigator Award N00014-12-1-0744, ONR MURI Grant N00014-12-1-0912, and by the Sloan Research Fellowship. H.R.O. is supported as a postdoctoral researcher by ONR MURI Grant N00014-12-1-0912. The authors thank A. Majda, M. Gehne, and two anonymous reviewers for their helpful comments.

#### REFERENCES

- Biello, J. A., and A. J. Majda, 2005: A new multiscale model for the Madden–Julian oscillation. *J. Atmos. Sci.*, **62**, 1694–1721, doi:10.1175/JAS3455.1.
- Cane, M. A., and S. E. Zebiak, 1985: A theory for El Niño and the Southern Oscillation. *Science*, **228**, 1085–1087, doi:10.1126/science.228.4703.1085.
- Chan, I. H., and T. G. Shepherd, 2013: Balance model for equatorial long waves. *J. Fluid Mech.*, **725**, 55–90, doi:10.1017/jfm.2013.146.
- , and —, 2014: Diabatic balance model for the equatorial atmosphere. *J. Atmos. Sci.*, **71**, 985–1001, doi:10.1175/JAS-D-13-0224.1.
- Chao, W. C., B. Yang, and X. Fu, 2009: A revised method of presenting wavenumber–frequency power spectrum diagrams that reveals the asymmetric nature of tropical large-scale waves. *Climate Dyn.*, **33**, 843–847, doi:10.1007/s00382-008-0494-3.
- Charney, J. G., 1963: A note on large-scale motions in the tropics. *J. Atmos. Sci.*, **20**, 607–609, doi:10.1175/1520-0469(1963)020<0607:ANOLSM>2.0.CO;2.
- Dee, D. P., and Coauthors, 2011: The ERA-Interim reanalysis: Configuration and performance of the data assimilation system. *Quart. J. Roy. Meteor. Soc.*, **137**, 553–597, doi:10.1002/qj.828.
- Dias, J., and G. N. Kiladis, 2014: Influence of the basic state zonal flow on convectively coupled equatorial waves. *Geophys. Res. Lett.*, **41**, 6904–6913, doi:10.1002/2014GL061476.
- Dutrifoy, A., and A. J. Majda, 2006: The dynamics of equatorial long waves: A singular limit with fast variable coefficients. *Commun. Math. Sci.*, **4**, 375–397, doi:10.4310/CMS.2006.v4.n2.a6.
- , and —, 2007: Fast wave averaging for the equatorial shallow water equations. *Commun. Partial Differ. Equations*, **32**, 1617–1642, doi:10.1080/03605300601188730.
- , S. Schochet, and A. J. Majda, 2009: A simple justification of the singular limit for equatorial shallow-water dynamics. *Commun. Pure Appl. Math.*, **62**, 322–333, doi:10.1002/cpa.20248.
- Fulton, S. R., and W. H. Schubert, 1985: Vertical normal mode transforms: Theory and application. *Mon. Wea. Rev.*, **113**, 647–658, doi:10.1175/1520-0493(1985)113<0647:VNMTA>2.0.CO;2.
- Gehne, M., and R. Kleeman, 2012: Spectral analysis of tropical atmospheric dynamical variables using a linear shallow-water modal decomposition. *J. Atmos. Sci.*, **69**, 2300–2316, doi:10.1175/JAS-D-10-05008.1.
- Gill, A. E., 1980: Some simple solutions for heat-induced tropical circulation. *Quart. J. Roy. Meteor. Soc.*, **106**, 447–462, doi:10.1002/qj.49710644905.
- Harvey, R., and W. Patzert, 1976: Deep current measurements suggest long waves in the eastern equatorial Pacific. *Science*, **193**, 883–885, doi:10.1126/science.193.4256.883.
- Heckley, W. A., and A. E. Gill, 1984: Some simple analytical solutions to the problem of forced equatorial long waves. *Quart. J. Roy. Meteor. Soc.*, **110**, 203–217, doi:10.1002/qj.49711046314.
- Hendon, H. H., and M. C. Wheeler, 2008: Some space–time spectral analyses of tropical convection and planetary-scale waves. *J. Atmos. Sci.*, **65**, 2936–2948, doi:10.1175/2008JAS2675.1.
- Kalnay, E., and Coauthors, 1996: The NCEP/NCAR 40-Year Reanalysis Project. *Bull. Amer. Meteor. Soc.*, **77**, 437–471, doi:10.1175/1520-0477(1996)077<0437:TNYRP>2.0.CO;2.
- Kasahara, A., 1976: Normal modes of ultralong waves in the atmosphere. *Mon. Wea. Rev.*, **104**, 669–690, doi:10.1175/1520-0493(1976)104<0669:NMOUWI>2.0.CO;2.
- , and K. Puri, 1981: Spectral representation of three-dimensional global data by expansion in normal mode functions. *Mon. Wea. Rev.*, **109**, 37–51, doi:10.1175/1520-0493(1981)109<0037:SROTDG>2.0.CO;2.
- Kiladis, G. N., M. C. Wheeler, P. T. Haertel, K. H. Straub, and P. E. Roundy, 2009: Convectively coupled equatorial waves. *Rev. Geophys.*, **47**, RG2003, doi:10.1029/2008RG000266.
- Legeckis, R., 1977: Long waves in the eastern equatorial Pacific Ocean: A view from a geostationary satellite. *Science*, **197**, 1179–1181, doi:10.1126/science.197.4309.1179.
- , W. Pichel, and G. Nesterczuk, 1983: Equatorial long waves in geostationary satellite observations and in a multichannel sea surface temperature analysis. *Bull. Amer. Meteor. Soc.*, **64**, 133–139, doi:10.1175/1520-0477(1983)064<0133:ELWIGS>2.0.CO;2.
- Lin, J.-L., M. Zhang, and B. Mapes, 2005: Zonal momentum budget of the Madden–Julian oscillation: The source and strength of equivalent linear damping. *J. Atmos. Sci.*, **62**, 2172–2188, doi:10.1175/JAS3471.1.
- , B. Mapes, and W. Han, 2008: What are the sources of mechanical damping in Matsuno–Gill-type models? *J. Climate*, **21**, 165–179, doi:10.1175/2007JCLI1546.1.
- Madden, R. A., 2007: Large-scale, free Rossby waves in the atmosphere—An update. *Tellus*, **59A**, 571–590, doi:10.1111/j.1600-0870.2007.00257.x.
- Majda, A. J., 2003: *Introduction to PDEs and Waves for the Atmosphere and Ocean*. Courant Lecture Notes in Mathematics, Vol. 9, American Mathematical Society, 234 pp.
- , and J. A. Biello, 2003: The nonlinear interaction of barotropic and equatorial baroclinic Rossby waves. *J. Atmos. Sci.*, **60**, 1809–1821, doi:10.1175/1520-0469(2003)060<1809:TNIOBA>2.0.CO;2.
- , and R. Klein, 2003: Systematic multiscale models for the tropics. *J. Atmos. Sci.*, **60**, 393–408, doi:10.1175/1520-0469(2003)060<0393:SMMFTT>2.0.CO;2.

- , and J. A. Biello, 2004: A multiscale model for tropical intraseasonal oscillations. *Proc. Natl. Acad. Sci. USA*, **101**, 4736–4741, doi:10.1073/pnas.0401034101.
- , and S. N. Stechmann, 2009: The skeleton of tropical intraseasonal oscillations. *Proc. Natl. Acad. Sci. USA*, **106**, 8417–8422, doi:10.1073/pnas.0903367106.
- Matsuno, T., 1966: Quasi-geostrophic motions in the equatorial area. *J. Meteor. Soc. Japan*, **44**, 25–42.
- Matthews, A. J., and R. A. Madden, 2000: Observed propagation and structure of the 33-h atmospheric Kelvin wave. *J. Atmos. Sci.*, **57**, 3488–3497, doi:10.1175/1520-0469(2000)057<3488:OPASOT>2.0.CO;2.
- Moncrieff, M. W., D. E. Waliser, M. J. Miller, M. A. Shapiro, G. R. Asrar, and J. Caughey, 2012: Multiscale convective organization and the YOTC virtual global field campaign. *Bull. Amer. Meteor. Soc.*, **93**, 1171–1187, doi:10.1175/BAMS-D-11-00233.1.
- Ogrosky, H. R., and S. N. Stechmann, 2015: The MJO skeleton model with observation-based background state and forcing. *Quart. J. Roy. Meteor. Soc.*, doi:10.1002/qj.2552, in press.
- Rommel, M., and L. Smith, 2009: New intermediate models for rotating shallow water and an investigation of the preference for anticyclones. *J. Fluid Mech.*, **635**, 321–359, doi:10.1017/S0022112009007897.
- Salby, M. L., 1984: Survey of planetary-scale traveling waves: The state of theory and observations. *Rev. Geophys. Space Phys.*, **22**, 209–236, doi:10.1029/RG022i002p00209.
- Schubert, W. H., L. G. Silvers, M. T. Masarik, and A. O. Gonzalez, 2009: A filtered model of tropical wave motions. *J. Adv. Model. Earth Syst.*, **1** (3), doi:10.3894/JAMES.2009.1.3.
- Sobel, A. H., J. Nilsson, and L. M. Polvani, 2001: The weak temperature gradient approximation and balanced tropical moisture waves. *J. Atmos. Sci.*, **58**, 3650–3665, doi:10.1175/1520-0469(2001)058<3650:TWTGAA>2.0.CO;2.
- Stechmann, S. N., and B. Stevens, 2010: Multiscale models for cumulus cloud dynamics. *J. Atmos. Sci.*, **67**, 3269–3285, doi:10.1175/2010JAS3380.1.
- , and H. R. Ogrosky, 2014: The Walker circulation, diabatic heating, and outgoing longwave radiation. *Geophys. Res. Lett.*, **41**, 9097–9105, doi:10.1002/2014GL062257.
- , and A. J. Majda, 2015: Identifying the skeleton of the Madden–Julian oscillation in observational data. *Mon. Wea. Rev.*, **143**, 395–416, doi:10.1175/MWR-D-14-00169.1.
- , —, and B. Khouider, 2008: Nonlinear dynamics of hydrostatic internal gravity waves. *Theor. Comput. Fluid Dyn.*, **22**, 407–432, doi:10.1007/s00162-008-0080-7.
- Stevens, D. E., H.-C. Kuo, W. H. Schubert, and P. E. Ciesielski, 1990: Quasi-balanced dynamics in the tropics. *J. Atmos. Sci.*, **47**, 2262–2273, doi:10.1175/1520-0469(1990)047<2262:QBDITT>2.0.CO;2.
- Tindall, J. C., J. Thuburn, and E. J. Highwood, 2006: Equatorial waves in the lower stratosphere. I: A novel detection method. *Quart. J. Roy. Meteor. Soc.*, **132**, 177–194, doi:10.1256/qj.04.152.
- Vallis, G. K., 2006: *Atmospheric and Oceanic Fluid Dynamics*. Cambridge University Press, 745 pp.
- Waliser, D. E., and Coauthors, 2012: The “year” of tropical convection (May 2008–April 2010). *Bull. Amer. Meteor. Soc.*, **93**, 1189–1218, doi:10.1175/2011BAMS3095.1.
- Wheeler, M., and G. N. Kiladis, 1999: Convectively coupled equatorial waves: Analysis of clouds and temperature in the wavenumber–frequency domain. *J. Atmos. Sci.*, **56**, 374–399, doi:10.1175/1520-0469(1999)056<0374:CCEWAO>2.0.CO;2.
- Yang, G.-Y., B. Hoskins, and J. Slingo, 2003: Convectively coupled equatorial waves: A new methodology for identifying wave structures in observational data. *J. Atmos. Sci.*, **60**, 1637–1654, doi:10.1175/1520-0469(2003)060<1637:CCEWAN>2.0.CO;2.
- , —, and —, 2007: Convectively coupled equatorial waves. Part I: Horizontal and vertical structures. *J. Atmos. Sci.*, **64**, 3406–3423, doi:10.1175/JAS4017.1.